A thesis submitted in partial fulfillment of the requirements for the degree Master of Science

Exploring the potential of quantum observables to search for new physics, in boosted top-pair production

Josue Salvador Elizalde Palacios
born in Irapuato, Guanajuato, Mexico

December 22, 2025

Fakultät Physik (Technische Universität Dortmund)

Dipartimento di Fisica e Astronomia (Università di Bologna)

École Universitaire de Physique et d'Ingénierie (Université Clermont Auvergne)

Abstract

This thesis explores the use of quantum observables in top–antitop production as probes of physics beyond the Standard Model. Particular emphasis is placed on spin correlations, an entanglement marker, and an asymmetry related to Bell inequalities. The analysis investigates how these observables behave in different kinematic regimes, from threshold to boosted top-quark events. It is shown that, especially in the boosted regions, quantum observables display enhanced sensitivity to new physics compared to traditional event-rate measurements. Within the framework of Effective Field Theory, deviations from the Standard Model are parametrized and confronted with CMS data on spin–correlation observables at high invariant mass. From this comparison, experimental limits on Wilson coefficients are extracted. The results provide competitive constraints on several operators while also highlighting directions in parameter space that remain weakly bounded, supporting the idea that quantum-inspired observables provide valuable input to LHC analyses

Contents

1 Introduction

Particle physics is concerned with the fundamental structure of nature. Our current understanding divides the constituents of the Universe at the most elementary level into fundamental particles and the interactions between them. The complete description of all presently known experimental data involving these particles is encapsulated in the Standard Model (SM) of particle physics, widely regarded as the most successful quantum field theory to date. For more than a decade, the SM has been thoroughly tested at the Large Hadron Collider (LHC), the world's most powerful particle accelerator, located at the European Organization for Nuclear Research (CERN).

Despite its remarkable success, the SM is incomplete. It describes only three of the four known fundamental forces: electromagnetism, the strong nuclear force, and the weak nuclear force, while leaving gravity entirely outside its framework. It also offers no explanation for dark matter, which is strongly supported by astrophysical and cosmological evidence, for the baryon asymmetry of the Universe, or for the origin of neutrino masses. Since the discovery of the Higgs boson at the LHC in 2012, no additional particles or unambiguous deviations from SM predictions have been observed in collider experiments, with the possible exception of neutrino masses, which require physics beyond the SM. Extensive searches for new physics continue across a wide range of experiments, yet the available energy scale remains a fundamental limitation.

This motivates the view of the SM as an effective theory valid only at currently accessible energy scales (up to ~ 13.6 TeV at the LHC) but ultraviolet (UV) incomplete. In this context, the Standard Model Effective Field Theory (SMEFT) provides a systematic framework to parametrise the effects of heavy new particles without producing them directly. SMEFT incorporates the particle content and symmetries of the SM while enabling the search for deviations from SM predictions in experiments such as the LHC.

Following the analysis in Ref. [1], this thesis studies possible deviations in quantum observables in top–antitop ($t\bar{t}$) events, specifically entanglement markers, Bell inequality violation parameters, and spin correlations. These observables can reveal the effects of certain SMEFT operators that are invisible in more common measurements such as total cross sections. They also help distinguish between different possible new physics scenarios that would otherwise be degenerate in other observables. Furthermore, some of these quantities can be measured with relatively high precision, and in certain energy regions SMEFT effects are amplified, making them especially sensitive to deviations from the SM.

The top quark, the heaviest known fundamental particle with a mass of $m_t = 172.52 \pm 0.33$ GeV, as reported by the ATLAS and CMS Collaborations [2], is an ideal probe for this kind of study because it decays before it hadronises and before any spin decorrelation

can happen, so information about its spin is directly transferred to its decay products and can be reconstructed from them. Due to this large mass, it also has the strongest coupling to the Higgs boson, making it particularly sensitive to many new physics effects predicted in SMEFT.

The top quarks, when produced in pairs, can be thoroughly studied at the LHC. The high cross-section and the characteristic topology of $t\bar{t}$ production allow this process to be isolated from backgrounds with good efficiency. This is especially true in the semi-leptonic final state, where one of the two top quarks includes a charged lepton and a neutrino in the final state. In this channel, the presence of two b-tagged jets together with the missing transverse energy (E_T^{miss}) provides a clean experimental signature. Several measurements of spin correlations, the spin density matrix, and entanglement in $t\bar{t}$ production have already been performed by the ATLAS and CMS collaborations [3–10]. As shown in these results, the precision is dominated by systematic uncertainties even in limited regions of the phase-space, with the only exception of the region where the system is produced with a very high $m_{t\bar{t}}$ mass. In this kinematic domain, SMEFT effects are expected to be enhanced, making it particularly interesting for the present analysis.

This thesis is organized as follows: Chapter 2 introduces the SM and the dynamics of top–quark pair production, with particular emphasis on their spin configurations. It then presents the quantum observables used throughout this analysis: spin correlations, the entanglement marker D_3, and the Bell inequality marker A^+. Finally, it introduces the SMEFT framework and the subset of dimension-six operators relevant to $t\bar{t}$ production and employed in this work. Chapter 3 describes the methodology: the Monte Carlo samples employed, the event selection strategy and the definition of complementary kinematic regions, the reconstruction of spin–correlation and quantum observables, their polynomial parametrization in terms of WCs, and the Bayesian inference setup implemented with the `EFTfitter` software tool. Chapter 4 presents the core results. It begins with sensitivity studies across the defined regions, highlighting the dependence of the observables on specific operators. It then compares the constraining power of different observables, presents the extracted posterior distributions and credible intervals for WCs, and derives limits using operator pairs effects. The most sensitive observables and regions are identified. Finally, CMS measurements of spin–correlation observables at high invariant mass are incorporated to derive experimental constraints on WCs, to compare the sensitivity of the two available kinematic domains, and to identify both the most constraining observables and the operators that remain weakly bounded. Chapter 5 summarizes the main findings and discusses their implications for future EFT studies with quantum-inspired observables in top–quark physics.

2 Theory

2.1 The Standard Model of Particle Physics

The SM is the current theoretical framework describing all known elementary particles and their interactions, with the exception of gravity. It is formulated as a gauge theory, meaning that its structure is dictated by requiring invariance of the Lagrangian under certain local symmetries, enforcing the symmetries forces the introduction of gauge fields, which in turn manifest physically as the carriers of the fundamental interactions. The set of local symmetries that define the SM is encoded in the gauge group

$$G_{SM} = \underbrace{\mathrm{SU}(3)_C}_{\text{strong}} \otimes \underbrace{\mathrm{SU}(2)_L \otimes \mathrm{U}(1)_Y}_{\text{electroweak}}, \tag{2.1}$$

where the indices C, L, and Y denote color, weak isospin, and weak hypercharge, respectively. Each factor of G_{SM} corresponds to one of the fundamental forces. Together, $SU(2)_L$ and $U(1)_Y$ describe the electroweak interaction (EWK), which unifies the weak force and electromagnetism, while $SU(3)_C$ governs the strong interaction, described by Quantum Chromodynamics (QCD) [11]. In practice, this means that the SM Lagrangian naturally separates into two parts: one describing the strong sector and the other the electroweak sector,

$$\mathcal{L}_{\text{SM}} = \mathcal{L}_{\text{QCD}} + \mathcal{L}_{\text{EWK}}. \tag{2.2}$$

Within the SM framework, matter particles, fermions with spin-$\frac{1}{2}$, interact by exchanging spin-one gauge bosons, which act as force carriers [11]. The fermions of the SM are divided into two groups: leptons and quarks, each arranged into three generations or families. To every fermion there corresponds an antiparticle with identical mass and spin but opposite internal quantum numbers

$$\textbf{Leptons:} \quad \begin{pmatrix} \nu_e \\ e \end{pmatrix}, \quad \begin{pmatrix} \nu_\mu \\ \mu \end{pmatrix}, \quad \begin{pmatrix} \nu_\tau \\ \tau \end{pmatrix} \tag{2.3}$$

$$\textbf{Quarks:} \quad \begin{pmatrix} u \\ d \end{pmatrix}, \quad \begin{pmatrix} c \\ s \end{pmatrix}, \quad \begin{pmatrix} t \\ b \end{pmatrix}. \tag{2.4}$$

The gauge bosons mediating their interactions are the gluon g, the photon γ, and the weak bosons W^+, W^- and Z. The Higgs boson H, completes the particle content of the SM, providing mass to elementary particles through the mechanism of spontaneous

symmetry breaking [11], explained in Section 2.1.2. The particles described by the SM are displayed in Fig. 2.1.
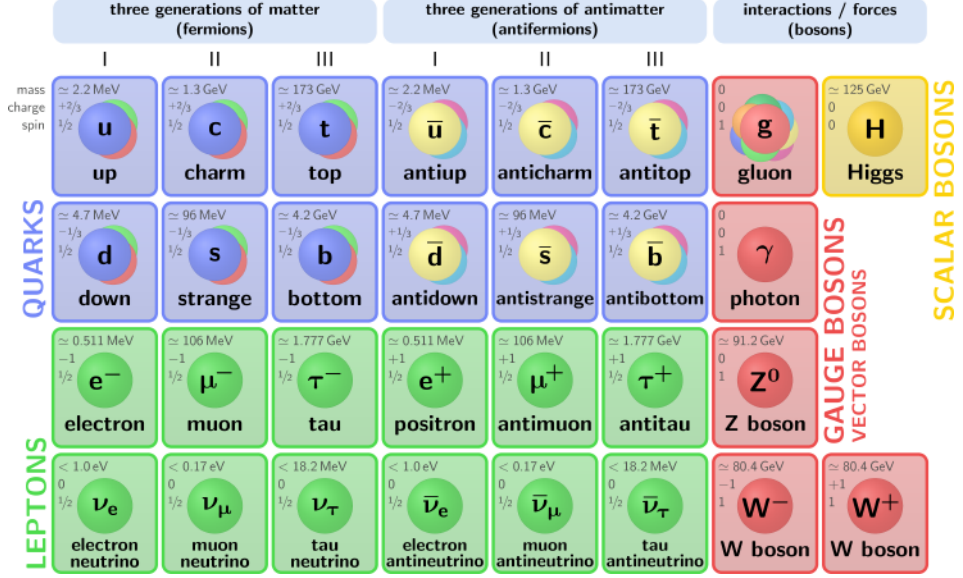
Figure 2.1: Elementary particles of the Standard Model, grouped into fermions, gauge bosons, and the Higgs boson [12].

2.1.1 Matter Content of the Standard Model

From a more formal perspective, the SM is a chiral gauge theory. This means that its matter content is described in terms of two-component Weyl spinors,

$$\psi = \begin{pmatrix} \psi_L \\ \psi_R \end{pmatrix}, \tag{2.5}$$

where ψ_L and ψ_R denote the left- and right-handed components. These components transform differently under the gauge group. The weak interaction is maximally chiral, since it couples only to left-handed fermions, while right-handed fermions do not participate [11]. The subscript L in $SU(2)_L$ reflects exactly this property.

Concretely, left-handed fermions are arranged in weak isospin doublets with $I = \frac{1}{2}$, whereas right-handed fermions are weak isospin singlets with $I = 0$ [13]. For instance, the quark doublets are written as

$$Q^i = \begin{pmatrix} u_L^i \\ d_L^i \end{pmatrix}, \tag{2.6}$$

and the lepton doublets as

$$L^i = \begin{pmatrix} \nu_L^i \\ e_L^i \end{pmatrix}, \tag{2.7}$$

where $i = 1, 2, 3$ labels the three generations and u_R^i, d_R^i, e_R^i are the singlets of $SU(2)_L$.

The pattern of electric charges follows directly from weak isospin. Up-type quarks (u, c, t) carry charge $Q = +2/3\,e$ and have third isospin component $I_3 = +1/2$, while down-type quarks (d, s, b) carry $Q = -1/3\,e$ with $I_3 = -1/2$. Likewise, neutrinos have $Q = 0$ and $I_3 = +1/2$, while charged leptons (e, μ, τ) have $Q = -1\,e$ and $I_3 = -1/2$.

The relation between electric charge Q, weak isospin I_3, and hypercharge Y is given by the Gell–Mann–Nishijima formula:

$$Q = I_3 + \tfrac{Y}{2}. \tag{2.8}$$

It is then convenient to summarize the transformation properties of matter fields under the gauge group G_{SM} of Eq. (2.1), in the compact notation (C, L, Y), where C refers to the color representation, L to weak isospin, and Y to hypercharge. The resulting assignments for quarks, leptons and the Higgs field are shown in Table 2.1.

Table 2.1: Matter content of the Standard Model. Each field is classified by its representation under the gauge group $(SU(3)_C, SU(2)_L, U(1)_Y)$ and by its spin [11].

Name	Label	(C, L, Y)	Spin
Quarks	$Q^i = \begin{pmatrix} u_L^i \\ d_L^i \end{pmatrix}$	$(\mathbf{3}, \mathbf{2}, +\frac{1}{6})$	$\frac{1}{2}$
	u_R^i	$(\bar{\mathbf{3}}, \mathbf{1}, +\frac{2}{3})$	$\frac{1}{2}$
	d_R^i	$(\bar{\mathbf{3}}, \mathbf{1}, -\frac{1}{3})$	$\frac{1}{2}$
Leptons	$L^i = \begin{pmatrix} \nu_L^i \\ e_L^i \end{pmatrix}$	$(\mathbf{1}, \mathbf{2}, -\frac{1}{2})$	$\frac{1}{2}$
	e_R^i	$(\mathbf{1}, \mathbf{1}, -1)$	$\frac{1}{2}$
Scalar	H	$(\mathbf{1}, \mathbf{2}, +\frac{1}{2})$	0

2.1.2 Gauge Bosons of the Standard Model

In the SM, the fundamental interactions are mediated by gauge bosons, which are associated with the gauge symmetries introduced in Eq. (2.1). Each factor of the gauge group contributes its own set of bosons, determined by the number of generators of the corresponding symmetry.

The strong interaction arises from the group $SU(3)_C$, which has eight generators T^A ($A = 1, \ldots, 8$) in the fundamental representation [11]. These are normalized as

$$\text{Tr}(T^A T^B) = \tfrac{1}{2}\,\delta^{AB}, \tag{2.9}$$

and correspond to the eight gluon fields $G_\mu^A(x)$.

The electroweak sector unifies the weak and electromagnetic interactions. The $SU(2)_L$ part has three generators, written as $\sigma^I/2$ ($I = 1, 2, 3$), which are associated with the weak gauge bosons W_μ^I. The $U(1)_Y$ part has a single generator Y, giving rise to the gauge field B_μ.

The physical electroweak bosons: photon A_μ, the Z_μ boson, and the charged $W_\mu^\pm$ bosons arise as linear combinations of the original gauge fields:

$$A_\mu(x) = \sin\theta_W\, W_\mu^3(x) + \cos\theta_W\, B_\mu(x), \tag{2.10}$$

$$Z_\mu(x) = \cos\theta_W\, W_\mu^3(x) - \sin\theta_W\, B_\mu(x), \tag{2.11}$$

$$W_\mu^\pm(x) = \frac{1}{\sqrt{2}}\left(W_\mu^1(x) \mp iW_\mu^2(x)\right). \tag{2.12}$$

Here, the weak mixing angle θ_W relates the coupling constant g of $SU(2)_L$ and the coupling constant g' of $U(1)_Y$:

$$\sin\theta_W = \frac{g'}{\sqrt{g^2 + g'^2}}, \quad \cos\theta_W = \frac{g}{\sqrt{g^2 + g'^2}}. \tag{2.13}$$

All gauge bosons of the SM are summarized in Table 2.2.

Table 2.2: Gauge bosons of the Standard Model with their representations under $SU(3)_C \times SU(2)_L \times U(1)_Y$ [11].

Name	Label	(C, L, Y)	Spin
Gluons	G_μ^A	$(\mathbf{8}, \mathbf{1}, 0)$	1
W/Z Bosons	$W_\mu^\pm, Z_\mu$	$(\mathbf{1}, \mathbf{3}, 0)$	1
Photon	A_μ	$(\mathbf{1}, \mathbf{1}, 0)$	1

Strong Interaction

Only quarks and gluons carry color charge, so they are the only particles that interact strongly. Color charge comes in three types (red, green, blue) and their corresponding anticolors. However, due to the phenomenon of *color confinement*, only color–neutral combinations are observed in nature. These include quark–antiquark pairs (mesons)

and three-quark states (baryons) [13]. In recent years, experiments at the LHCb have also provided evidence for exotic hadrons, such as four-quark (tetraquark) and five-quark (pentaquark) bound states [14, 15]. In high-energy collisions, confinement manifests through the process of *hadronization*, where quarks and gluons produced at short distances cannot remain isolated and instead evolve into observable colorless states, appearing in detectors as jets of hadrons.

The theoretical description of these phenomena is provided by QCD, whose Lagrangian can be written as

$$\mathcal{L}_{\text{QCD}} = -\frac{1}{4} G^A_{\mu\nu} G^{\mu\nu,A} + \bar{q} \left(i\gamma^\mu D_\mu - m \right) q, \tag{2.14}$$

where q represents the quark field, $\bar{q}$ their Dirac adjoint and m its mass. The covariant derivative D_μ and the field-strength tensor $G^A_{\mu\nu}(x)$ are defined as

$$D_\mu = \partial_\mu + i g_S T^A G^A_\mu(x), \tag{2.15}$$

$$G^A_{\mu\nu}(x) = \partial_\mu G^A_\nu(x) - \partial_\nu G^A_\mu(x) + g_S f^{ABC} G^B_\mu(x) \, G^C_\nu(x), \tag{2.16}$$

where g_S is the strong coupling constant and f^{ABC} are the structure constants of $SU(3)_C$.

Under a local $SU(3)_C$ gauge transformation, the quark fields transform as

$$q \;\longrightarrow\; U(x)\, q \;=\; e^{i g_S \, \alpha^A(x) T^A} \, q, \tag{2.17}$$

where $\alpha^A(x)$ are arbitrary space-time dependent parameters. The gluon fields transform as

$$G^A_\mu(x) \;\longrightarrow\; G^A_\mu(x) - \frac{1}{g_S} \, \partial_\mu \alpha^A(x) - f^{ABC} \, \alpha^B(x) \, G^C_\mu(x), \tag{2.18}$$

reflecting the non-Abelian nature of QCD, which implies that gluons are self-interacting due to the presence of the f^{ABC} term.

Electroweak Interaction

The weak force is responsible for processes that change the flavor of elementary particles. In the Standard Model, the weak force and electromagnetism combine into the electroweak force. The electroweak Lagrangian is

$$\mathcal{L}_{\text{EWK}} = -\frac{1}{4} W^a_{\mu\nu} W^{a\mu\nu} - \frac{1}{4} B_{\mu\nu} B^{\mu\nu} + i\bar{\psi}\gamma^\mu D_\mu \psi, \tag{2.19}$$

with field-strength tensors

$$B_{\mu\nu} = \partial_\mu B_\nu - \partial_\nu B_\mu, \tag{2.20}$$

$$W^a_{\mu\nu} = \partial_\mu W^a_\nu - \partial_\nu W^a_\mu - g \, \epsilon^{abc} W^b_\mu W^c_\nu, \tag{2.21}$$

and the covariant derivative

$$D_\mu = \partial_\mu + i g \, W^I_\mu \sigma_I + i \frac{g'}{2} B_\mu Y. \tag{2.22}$$

The $U(1)_Y$ symmetry acts on both chiralities as

$$\psi_{L,R} \longrightarrow e^{i\alpha(x)Y/2} \psi_{L,R}, \tag{2.23}$$

while $SU(2)_L$ acts only on left-handed fermions,

$$\psi_L \longrightarrow e^{i\beta_I(x)\sigma^I/2} \psi_L, \tag{2.24}$$

where σ^I are the Pauli matrices.

The $SU(2)_L \otimes U(1)_Y$ gauge symmetry forbids explicit mass terms for $W^\pm$ and Z, requiring spontaneous electroweak symmetry breaking to explain their observed masses.

Spontaneous Symmetry Breaking

A key feature of the SM is spontaneous symmetry breaking (SSB). Although the electroweak sector is originally symmetric under $SU(2)_L \otimes U(1)_Y$, the vacuum of the theory is not. This occurs when the Higgs field acquires a nonzero vacuum expectation value, breaking the symmetry down to $U(1)_{\text{EM}}$. As a consequence, the weak bosons $W^\pm$ and Z become massive, while the photon remains massless. At the same time, fermions acquire mass through their couplings to the Higgs field [13]. SSB therefore explains both the short range of the weak interaction and the origin of particle masses within the SM.

2.2 The Top Quark

The top quark was theorized by Makoto Kobayashi and Toshihide Maskawa in 1973 as part of the mechanism explaining CP violation in the SM through the introduction of a third quark generation [16], and discovered jointly by the CDF and D0 collaborations at the Fermilab Tevatron collider in 1995 [17, 18].

It is the heaviest fundamental particle of the SM, with a mass of

$$m_t = 172.52 \pm 0.33 \,\text{GeV}, \tag{2.25}$$

as reported by the ATLAS and CMS Collaborations [2]. The corresponding total decay width is $\Gamma_t = 1.41 \pm 0.02 \,\text{GeV}$ [19], which implies a lifetime of

$$\tau_t = \frac{\hbar}{\Gamma_t} \approx 4.9 \times 10^{-25} \,\text{s}, \tag{2.26}$$

much shorter than the hadronization timescale of QCD ($\sim 10^{-23} \,\text{s}$) [19]. This feature is extremely useful for the study of spin related quantum effects, since the top quark decays before hadronization and thus its spin information is directly preserved in its decay products [20].

In the proton-proton collisions at the LHC, top quarks are most likely produced in top-anti-top quark pairs, via strong interaction. At leading order, the production mechanisms are gluon–gluon fusion and quark–antiquark annihilation, where gluon–gluon fusion dominates with about $\sim 90\%$ of the total cross section at LHC energies. The corresponding Feynman diagrams are shown in Figure 2.2.


(a) Gluon–gluon fusion.

(b) Quark–antiquark annihilation.
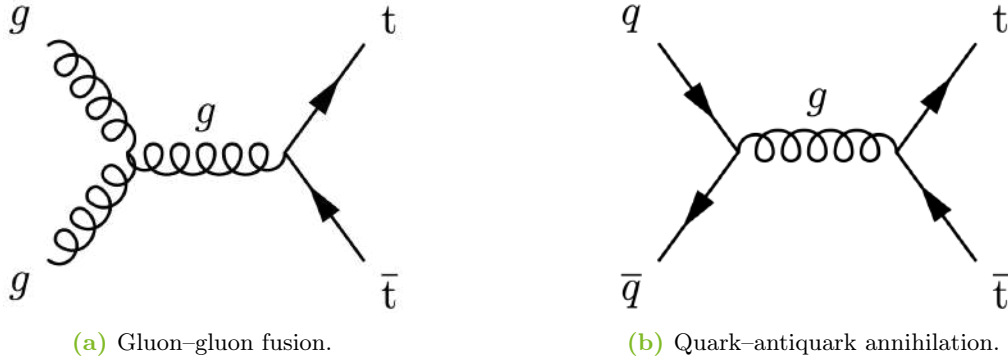
Figure 2.2: Leading order Feynman diagrams for top quark pair production in proton–proton collisions at the LHC.

The top quark decays almost exclusively into a b quark and a W boson, this can be understood by looking at the elements of the Cabibbo–Kobayashi–Maskawa (CKM) matrix, which can be used to determine the probability of a top quark decaying into either d, s, or b quark. In particular, the value for the element relating the decay of top quark into b quark is $|V_{tb}| \simeq 1$. The W boson can subsequently decay either leptonically, into a charged lepton and its associated neutrino, or hadronically, into a quark–antiquark pair. The corresponding branching ratios are illustrated in Figure 2.3.
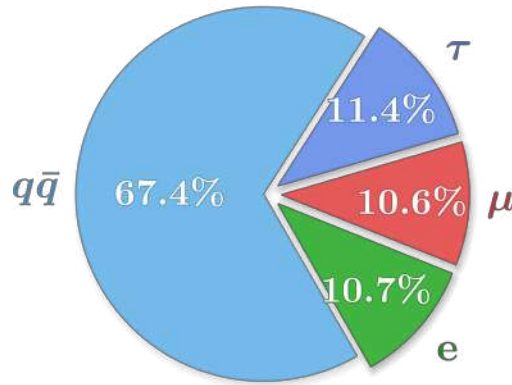
Figure 2.3: Pie chart of the W decay channels. The hadronic decay is shown in blue, while the three different leptonic decays are shown in purple, red and green [12].

In this thesis, the focus is on the semileptonic decay channel, which provides a good compromise between statistics and background contamination: it features a larger rate than the dileptonic channel and a cleaner final state than the fully hadronic channel. The topology of this channel is sketched in Figure 2.4.
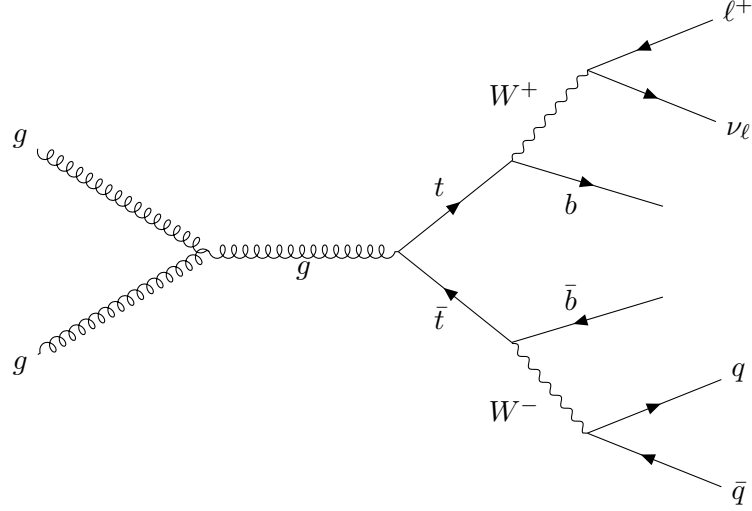
Figure 2.4: Feynman diagram of semi-leptonic channel in $t\bar{t}$ production with a final positive charged lepton.

It corresponds to events where one of the W bosons from the $t\bar{t}$ pair decays leptonically ($W \to \ell\nu_\ell$), while the other decays hadronically ($W \to q\bar{q}'$). No distinction is made between the case in which the leptonic W originates from the top or the anti-top quark, both possibilities are included in this work. In the case of $W \to \tau\nu_\tau$, only those events where $\tau \to e\,\nu_e\,\nu_\tau$ or $\tau \to \mu\,\nu_\mu\,\nu_\tau$ are used.

2.2.1 Spin in Top-Quark Pair Production

Spin is an intrinsic form of angular momentum carried by elementary particles. It is a purely quantum property, measured in units of the reduced Planck's constant $\hbar$. The spin of a particle is quantized to

$$s = 0, \tfrac{1}{2}, 1, \tfrac{3}{2}, 2, \dots$$

As mentioned earlier, fermions, such as the top quark, have spin $s = \frac{1}{2}$. Their spin degrees of freedom correspond to a two-level quantum system with two possible states, usually denoted as "up" with $|\uparrow\rangle$ and "down" with $|\downarrow\rangle$ relative to a chosen quantization axis.

In quantum mechanics, the state of a system is usually represented by a vector like $|\uparrow\rangle$ or $|\downarrow\rangle$ in Hilbert space. However, in realistic situations such as those at the LHC,

the relevant description involves statistical mixtures of pure states. The most general description of such a mixed state is given by the density matrix formalism. The density matrix of a system is defined as,

$$\rho = \sum_j p_j \, |\psi_j\rangle\langle\psi_j|, \tag{2.27}$$

where each $|\psi_j\rangle$ is a possible pure state of the system and p_j is the probability of that state, with $\sum_j p_j = 1$ [21]. A pure state corresponds to the case where one of the p_j is 1 and all others are 0, in this case the density operator satisfies $\rho^2 = \rho$. Any deviation from this, or equivalently $\text{Tr}[\rho^2] < 1$, indicates a mixed state, which represents incomplete knowledge about the actual pure state of the system.

For a single spin-1/2 particle, the density matrix can be parametrized as

$$\rho = \tfrac{1}{2} \left(\mathbb{1} + \sum_{i=1}^{3} B_i \sigma_i \right), \tag{2.28}$$

where $\mathbb{1}$ denotes the 2×2 identity matrix, σ_i are the Pauli matrices, and $B_i \in \mathbb{R}$ are the components of the Bloch vector $\mathbf{B}$. The vector $\mathbf{B}$ encodes the expectation values of the spin along the three orthogonal axes, with $|\mathbf{B}| \leq 1$. Geometrically, $\mathbf{B}$ lies inside or on the Bloch sphere: pure states correspond to vectors on the surface, $|\mathbf{B}| = 1$, while mixed states are represented by vectors strictly inside the sphere, $|\mathbf{B}| < 1$, this is represented in Fig. 2.5.
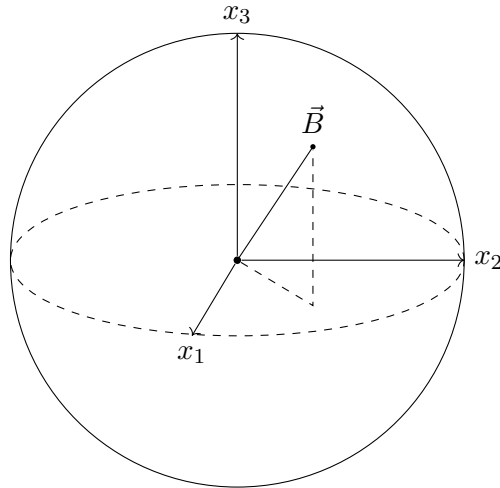
Figure 2.5: Representation of a spin-$\frac{1}{2}$ state on the Bloch sphere [12].

When considering a system of two spin-$\frac{1}{2}$ particles, the joint Hilbert space has total dimension four, with the standard product basis

$$\{|\uparrow\uparrow\rangle,\ |\uparrow\downarrow\rangle,\ |\downarrow\uparrow\rangle,\ |\downarrow\downarrow\rangle\}.$$

However, it is often convenient to choose a basis consisting of the eigenstates of the total spin operators

$$(\mathbf{S}^{\text{tot}})^2 = (\mathbf{S} + \bar{\mathbf{S}})^2, \qquad S_i^{\text{tot}} = S_i + \bar{S}_i,$$

where $\mathbf{S} = (S_1, S_2, S_3)$ acts on the first particle, and $\bar{\mathbf{S}} = (\bar{S}_1, \bar{S}_2, \bar{S}_3)$ acts on the second particle. This decomposition yields two distinct multiplets:

- **Singlet state** $^1S_0$ ($S = 0$, $m_S = 0$):

$$|0,0\rangle = \tfrac{1}{\sqrt{2}}\big(|\uparrow\downarrow\rangle - |\downarrow\uparrow\rangle\big).$$

- **Triplet states** $^3S_1$ ($S = 1$, $m_S = +1, 0, -1$):

$$|1,1\rangle = |\uparrow\uparrow\rangle, \qquad |1,-1\rangle = |\downarrow\downarrow\rangle, \qquad |1,0\rangle = \tfrac{1}{\sqrt{2}}\big(|\uparrow\downarrow\rangle + |\downarrow\uparrow\rangle\big).$$

In the case of top–antitop production at the LHC, the strong interaction dynamics select characteristic spin configurations depending on the initial state and on the kinematics of the event. For quark–antiquark annihilation, the $t\bar{t}$ system is dominantly produced in a triplet $^3S_1$ separable states $|\uparrow\uparrow\rangle$ and $|\downarrow\downarrow\rangle$ near threshold [22]. In contrast, gluon–gluon fusion allows for both singlet and triplet configurations: close to threshold the dominant contribution is the singlet $^1S_0$, whereas at high invariant masses $m_{t\bar{t}}$ the production is dominated by triplet states with opposite spins, analogous to the $q\bar{q}$ channel [22].

This implies that both singlet and triplet states are realized in proton–proton collisions at the LHC. The interplay of these channels gives rise to non–trivial spin correlations, which can be probed experimentally through the angular distributions of the top quark decay products. The density matrix of a top–antitop pair system is given by

$$\rho = \frac{1}{4}\left(\mathbb{1}\otimes\mathbb{1} + \sum_{i=1}^{3} B_i\sigma_i\otimes\mathbb{1} + \sum_{j=1}^{3}\bar{B}_j\mathbb{1}\otimes\sigma_j + \sum_{i=1}^{3}\sum_{j=1}^{3} C_{ij}\sigma_i\otimes\sigma_j\right), \qquad (2.29)$$

with B and $\bar{B}$ describing the polarization of the top and antitop quarks, respectively, while the coefficients C_{ij} encode their spin correlations. The indices $i, j = 1, 2, 3$ correspond to spin components along a chosen orthonormal basis $\{\hat{e}_1, \hat{e}_2, \hat{e}_3\}$ in the reference frame under consideration.

The coefficients C_{ij} presented here depend strongly on the kinematics of the $t\bar{t}$ system and on the chosen reference frame. In particular, strong $t\bar{t}$ production preserves both P and CP symmetries, which implies $B_i = \bar{B}_i = 0$ and $C_{ij} = C_{ji}$ [20]. In combination with a suitable choice of reference frame, this can reduce the spin–density matrix of the top–antitop system to a form simpler than that of Eq. 2.29.

Spin Analysing Power

The spin analysing power quantifies how strongly a given decay product reflects the spin orientation of the parent top quark. Thanks to the fully chiral nature of weak interactions, the momenta of the daughter particles of the top quark and the fermions from the subsequent W decay are correlated with the spin of the initial top quark. The decay width at leading order is given by:

$$\frac{1}{\Gamma}\frac{d\Gamma}{d\cos\theta_X} = \frac{1 + \alpha_X \cos\theta_X}{2},$$

where α_X is the spin analysing power of the decay product X and θ_X is the angle between the top-quark spin and the momentum of X in the top rest frame [1].

Since the top quark decays before hadronization, its spin information is preserved and imprinted in the angular distributions of its decay products. Different final states carry different sensitivity [20]: for the charged lepton ℓ^+ or the $\bar{d}$-quark, one has $\alpha_d = +1$; for the neutrino $\bar{\nu}$ and the u-quark, $\alpha_u = -0.3$. In the case of the b-quark, the coefficient is about $\alpha_b = -0.4$, while for the W^+ boson it is $\alpha_{W^+} = +0.4$. For anti-top decays, the signs of all these coefficients are reversed. This is summarized in Table 2.3.

	b quark	W^+ boson	$\ell^+/\bar{d}$ quark	$\bar{\nu}/u$ quark	Hadronic Pol.	Soft
α_i (LO)	-0.4	0.4	1	1	0.64	0.5

Table 2.3: Standard Model predictions of the spin analysing power at LO for the decay products of the top quark. The corresponding decay products of the anti-top quark have a reversed sign [23–25].

This feature is crucial for experimental analyses of $t\bar{t}$ events. In practice, charged leptons are usually chosen as spin analyzers, since they provide the cleanest experimental signature and the strongest sensitivity to the underlying spin correlations. Analogous to the charged lepton, the down–type quark would in principle be the optimal spin analyzer, as it also carries maximal spin-analyzing power. However, at detector level it is impossible to directly identify the down–type quark, because the jets produced in hadronic decays of the W cannot be unambiguously traced back to a specific light quark.

For this reason, experimental analyses rely on proxy observables: a commonly used choice is the "soft" method, which takes the less energetic of the two light jets from the top decay in the top quark rest frame as an approximate direction of the down–type quark, yielding a reduced but still significant analyzing power $\alpha_{\mathrm{soft}} \approx 0.5$ [20, 24]. A more refined approach is the hadronic polarimeter, which assigns probabilities to each jet of being the down–type quark based on their kinematics and combines them into an effective spin-analyzer direction, reaching $\alpha_{\mathrm{opt}} \approx 0.64$ [20, 25]. In this work, charged leptons are used as the main spin analyzers, and the down-type quark is considered at parton level in

order to illustrate the maximal spin sensitivity achievable in principle.

Determination of the Spin State

As discussed previously, the spin state of the $t\bar{t}$ system can be reconstructed from the angular distributions of its decay products. These distributions provide direct access to the polarization of the individual top quarks and to their mutual spin correlations, which are encoded in the coefficients B_i, $\bar{B}_i$, and C_{ij}.

The differential cross-section for the process $pp \to t\bar{t} \to ab$, where a (b) is a decay product of the top (anti-top) quark, can be expressed as a function of angular distributions as [26]

$$\frac{1}{\sigma} \frac{d\sigma}{d\cos\theta_i^+} = \frac{1}{2}\left(1 + \alpha_a B_i \cos\theta_i^+\right), \tag{2.30}$$

$$\frac{1}{\sigma} \frac{d\sigma}{d\cos\theta_i^-} = \frac{1}{2}\left(1 + \alpha_b \bar{B}_i \cos\theta_i^-\right), \tag{2.31}$$

In Eqs. (2.30) and (2.31), θ_i^+ (θ_i^-) is the angle between the momentum of the decay product a (b) and the i-th quantization axis in the top (anti-top) rest frame. The coefficients α_a and α_b are the spin analyzing powers of the final-state particles. The parameters B_i and $\bar{B}_i$ encode the degree of spin polarization along the i-th axis for the top and anti-top, respectively.

$$\frac{1}{\sigma} \frac{d\sigma}{d(\cos\theta_i^+, \cos\theta_j^-)} = -\frac{1 + C_{ij}\,\alpha_a\alpha_b\,\cos\theta_i^+ \cos\theta_j^-}{2} \log\left|\cos\theta_i^+ \cos\theta_j^-\right|. \tag{2.32}$$

Equation (2.32) gives the differential cross section in terms of the product $\cos\theta_i^+ \cos\theta_j^-$. This expression is particularly useful for probing spin entanglement and measuring deviations from Standard Model predictions in $t\bar{t}$ production. Integration of the above differential cross-sections gives the relations for the individual polarization of the top anti-top quarks [1]

$$B_i = \left\langle \frac{3}{\alpha_a} \cos\theta_i^+ \right\rangle, \quad \bar{B}_i = \left\langle \frac{3}{\alpha_b} \cos\theta_i^- \right\rangle, \tag{2.33}$$

as well as the spin correlation coefficients between the tops

$$C_{ij} = \left\langle \frac{9}{\alpha_a\alpha_b} \cos\theta_i^+ \cos\theta_j^- \right\rangle. \tag{2.34}$$

The expectation value of a generic observable s is given by

$$\langle s \rangle = \frac{\int s\, |\mathcal{M}|^2\, d\Pi}{\int |\mathcal{M}|^2\, d\Pi} \equiv \frac{\sigma_s}{\sigma}, \tag{2.35}$$

where $|\mathcal{M}|^2$ denotes the squared transition matrix element for the process under consideration and $d\Pi$ is the Lorentz-invariant phase-space element. The numerator defines the cross-section weighted by the observable s, denoted as σ_s, while the denominator is the total cross-section σ.

The Helicity Basis

A suitable reference frame to study spin correlations in top-quark pair production is the helicity basis $\{\hat{k}, \hat{r}, \hat{n}\}$, defined in the $t\bar{t}$ rest frame. In this basis, the axes are constructed as follows [1]: The first axis, $\hat{k}$, is taken along the direction of motion of the top quark. The second axis, $\hat{r}$, lies in the scattering plane, which is spanned by the beam axis $\hat{p}$ and the top momentum. Finally, the third axis, $\hat{n}$, is perpendicular to the scattering plane. θ is the scattering angle of the top (or anti-top) quark in the center-of-mass frame of the $t\bar{t}$ system.

$$\hat{k} = \text{top quark direction}, \qquad \hat{r} = \frac{\hat{p} - \hat{k}\cos\theta}{\sin\theta}, \qquad \hat{n} = \frac{\hat{p} \times \hat{k}}{\sin\theta}. \tag{2.36}$$

The helicity basis is represented in Fig. 2.6, where a charged lepton ℓ^- is produced from the decay of the top quark. Its direction in the top rest frame can be characterized by the angles θ_k^-, θ_n^- and θ_r^-, which are defined with respect to the k-, n- and r-axes of the helicity basis, respectively.
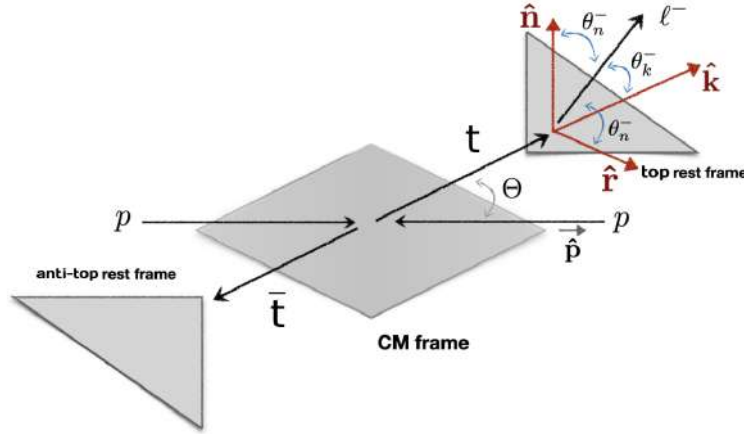

Figure 2.6: Unit vectors and momenta in the Center of Mass (CM) of after proton-proton, with the helicity basis of top quark. Recreated from [27].

This choice is particularly well-suited for top-quark physics at the LHC. In the helicity basis, the spin-correlation matrix becomes approximately diagonal, which means that the

dominant coefficients C_{kk}, C_{rr}, C_{nn} directly encode the correlations along the longitudinal, transverse, and normal directions, respectively [1, 20]. In particular, the invariant mass $m_{t\bar{t}}$ of the top-antitop pair and $\cos\theta$ are key variables. As a result, the spin-correlation observables C_{ij} show a non-trivial dependence on both $m_{t\bar{t}}$ and $\cos\theta$, as illustrated for the diagonal terms C_{ii} in the helicity basis in Fig. 2.7 and Fig. 2.8.

(a) C_{ii} as a function of $m(t\bar{t})$.

(b) C_{ii} as a function of $m(t\bar{t})$ with $|\cos(\theta)| < 0.4$.
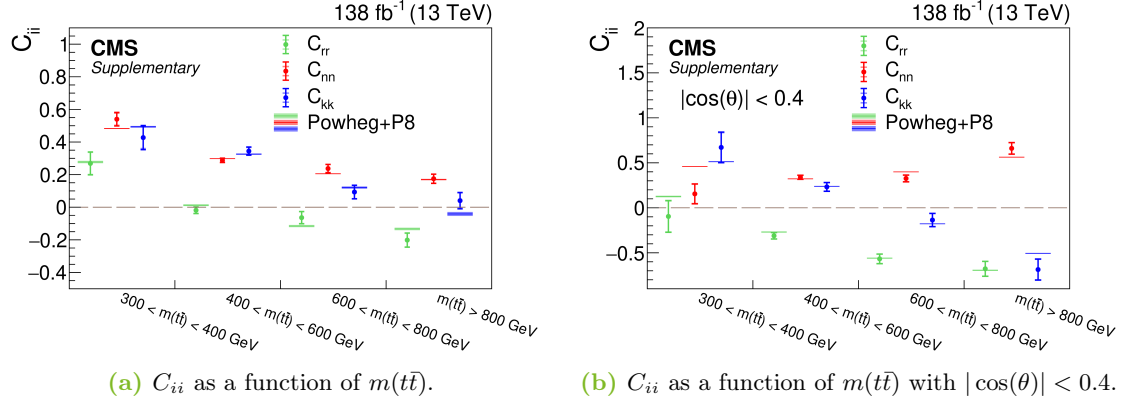
Figure 2.7: Diagonal coefficients C_{ii} in bins of $m_{t\bar{t}}$, measured with proton–proton collision data at $\sqrt{s} = 13$ TeV collected by the CMS experiment [28]. The markers represent the measured values, with inner error bars indicating statistical uncertainties and outer error bars representing total uncertainties. The results are compared with predictions from POWHEG+PYTHIA.
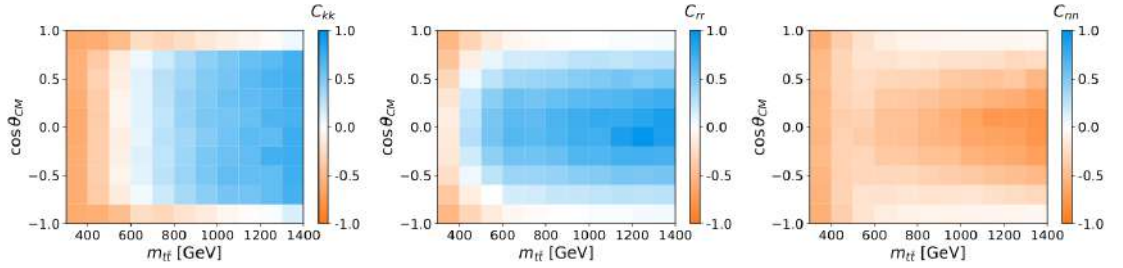
Figure 2.8: Distributions at parton level for the coefficients C_{kk} (left), C_{rr} (middle), and C_{nn} (right), evaluated in the helicity frame as functions of $(m_{t\bar{t}}, \cos\theta_{CM})$. Figure taken from Ref. [20]

2.2.2 Entanglement and Bell Inequalities in Top-Quark Pair Production

In the context of $t\bar{t}$ production, entanglement refers to the existence of non-separable quantum states in which the spin degrees of freedom of the top and anti-top quarks

cannot be described independently, but only through their joint density matrix [29]. Such correlations go beyond any classical probabilistic mixture and constitute a purely quantum feature. A stronger form of quantum nonlocality can be probed through Bell inequalities, which provide experimentally testable bounds that all local hidden-variable theories must satisfy [20, 30]. Their violation implies the impossibility of a classical description of the correlations. In the case of top-quark pair production, certain observables can act as entanglement or Bell markers without requiring the full reconstruction of the density matrix of the system, thereby enabling tests of separability and potential Bell inequality violation in a more efficient way and with reduced statistical uncertainty.

Entanglement marker

A particularly useful way to quantify the global degree of spin correlation in top-quark pair production and a probe of quantum entanglement in top–quark pair production, is through the observable D_3, defined as [29, 31]:

$$D_3 := -\frac{1}{3}(C_{11} + C_{22} - C_{33}) = -\frac{1}{3}\text{Tr}[CP_3] \tag{2.37}$$

with $P_3 = \text{diag}(1, 1, -1)$, corresponding to a reflection of the third axis in the anti–top rest frame. In the helicity basis it has the form

$$D_3 = -\tfrac{1}{3}(C_{kk} + C_{rr} - C_{nn}). \tag{2.38}$$

Experimentally this observable can be extracted from the normalized distribution of the reflected opening angle θ'_{ab} between the spin analyzers a and b, defined with their corresponding unit vector momenta $\hat{\boldsymbol{p}}_a, \hat{\boldsymbol{p}}_b$ as $\cos\theta'_{ab} \equiv \hat{\boldsymbol{p}}_a \cdot (P_3\,\hat{\boldsymbol{p}}_b)$. The distribution is

$$\frac{1}{\sigma}\frac{d\sigma}{d\cos\theta'_{ab}} = \frac{1}{2}\big(1 - \alpha_a\alpha_b\,D_3\cos\theta'_{ab}\big), \tag{2.39}$$

with $\alpha_{a,b}$ the spin analyzing powers. This yields

$$D_3 = -\left\langle \frac{3}{\alpha_a\alpha_b}\cos\theta'_{ab} \right\rangle. \tag{2.40}$$

This scalar quantity is particularly useful in the boosted regime where it serves as an entanglement marker. Measuring D_3 gives a direct possibility to verify if a state is entangled without having to reconstruct each C_{ii} separately, reducing statistical uncertainty [31]. The condition can be expressed directly as

$$D_3 > \frac{1}{3}$$

for entanglement. Therefore, a measurement of D_3 below this threshold provides unambiguous experimental evidence that the top-antitop spin state is non-separable and genuinely entangled.

Bell inequality marker

The observable A^+, called asymmetry, is defined within the spin-correlation formalism as a projection of the correlation matrix C_{ij} onto the two axes transverse to the helicity direction. Following Ref. [29, 31], one finds

$$A^+ = \frac{\pi}{16} \, \alpha_a \alpha_b \, (C_{11} + C_{22}) \,, \tag{2.41}$$

with C_{11} and C_{22} spin-correlation coefficients, and $\alpha_{a,b}$ are the spin-analyzing powers of the decay.

A^+ can be regarded as a direct experimental probe of Bell inequality violation in top–quark pair production. In the helicity basis it takes the form

$$A^+ = \frac{\pi}{16} \, \alpha_a \alpha_b \, (C_{kk} + C_{rr}) \tag{2.42}$$

In this way, A^+ serves as a compact Bell marker without reconstructing individual C_{ij}, directly linked to the CHSH inequality in the helicity basis. Combining A^+ with D_3 together allow to discriminate separable from entangled states. In practice, A^+ serves as a Bell marker and, together with D_3, offers an experimentally accessible and more robust test to confirm the presence of entanglement in top-quark pair production.

At the LHC it is already possible to demonstrate that top–quark pairs are produced in an entangled quantum state. However, the violation of a Bell inequality is much more difficult. In theory, when the tops are produced with very high energy ($m_{t\bar{t}} \gtrsim 1.5$ TeV), the correlations are strong enough to violate the classical CHSH bound. In practice, the number of events in this kinematic region is very small, and the experimental uncertainties are large. As a result, the LHC can realistically establish the presence of entanglement at the TeV scale, but we think is impossible to proof of Bell inequality violation.

2.3 The Standard Model as an Effective Field Theory

The SM of particle physics, while remarkably successful, leaves fundamental phenomena unexplained, such as the existence of dark matter, the observed matter–antimatter asymmetry, and the absence of gravity from the theory. These shortcomings strongly suggest the presence of new physics beyond the SM, potentially arising from new particles or interactions. Since different open problems may require different theoretical extensions, a wide variety of beyond-the-SM scenarios have been proposed.

A powerful way to address these possibilities in a unified manner is through a model-independent framework. Effective Field Theories (EFTs) provide such an approach by describing the low-energy effects of an unknown fundamental theory with characteristic scale Λ. At energies well below Λ, heavy states with masses of order Λ cannot be directly produced, and the presence of new physics appears only through small deviations in the interactions of known particles.

Within this formalism, the Standard Model Effective Field Theory (SMEFT) extends the SM Lagrangian by including all higher-dimensional operators consistent with the SM symmetries, suppressed by powers of $\frac{1}{\Lambda}$. For sufficiently large Λ, the resulting new-physics contributions are naturally small and can be treated as perturbative corrections to the SM predictions [1].

2.3.1 SMEFT

The most general Lagrangian that is Lorentz invariant and invariant under the Standard Model (SM) gauge group $SU(3)_C \times SU(2)_L \times U(1)_Y$, and that reproduces the SM at low energies, is given by [1]:

$$\mathcal{L}_{\text{SMEFT}} = \mathcal{L}_{\text{SM}} + \sum_{d=5}^{\infty} \sum_{k} \frac{c_k^{(d)}}{\Lambda^{d-4}} \mathcal{O}_k^{(d)}, \tag{2.43}$$

where $c_k^{(d)}$ are called Wilson Coefficients (WCs) of the dimension-d operators $\mathcal{O}_k^{(d)}$, and Λ denotes the characteristic energy scale of new physics, typically $\Lambda \sim 1\text{--}10$ TeV.

The effects of dimension-six operators on observables can be parametrized as follows:

$$\sigma(C_i) = \sigma_{\text{SM}} + \frac{1}{\Lambda^2}\,\sigma_{\text{SM-EFT}} + \frac{1}{\Lambda^4}\,\sigma_{\text{EFT}}, \tag{2.44}$$

where the $\mathcal{O}(1/\Lambda^2)$ terms arise from the interference between Standard Model and EFT amplitudes, while the $\mathcal{O}(1/\Lambda^4)$ terms originate from the squared EFT contributions. These include both quadratic terms $\mathcal{O}(C_i^2)$ and mixed contributions $\mathcal{O}(C_i C_j)$ from different Wilson coefficients. In this analysis, the impact of these operators on spin correlations and other relevant observables is studied at both linear and quadratic order in the effective expansion, i.e. $\mathcal{O}(c/\Lambda^2)$ and $\mathcal{O}(c^2/\Lambda^4)$.

The top quark plays a special role in the search for new physics. It is the only quark with a Yukawa coupling to the Higgs of order unity. This property suggests that the top quark is deeply connected to the mechanism of electroweak symmetry breaking, and that any new interaction in this sector may manifest in top physics. Combined with its extremely short lifetime, the top quark provides a unique laboratory to test the SM at the electroweak scale and potentially uncover subtle effects of new physics within the SMEFT framework.

2.3.2 Dimension-6 Operators in Top-pair Production

The number of independent dimension-6 operators is very large. In the so-called Warsaw basis there are 2499 possible operators, but only a small subset has a significant impact on a specific process. This analysis focuses on dimension-six operators that contain at least one top quark and contribute to $t\bar{t}$ production. Each operator typically modifies

one or a few couplings in the Feynman diagrams, or introduces new effective vertices, thereby altering production rates or observable kinematic distributions. In particular, for $t\bar{t}$ production via QCD, three classes of couplings are especially relevant to EFT corrections [29, 32]:

- **Purely gluonic vertices:** interactions involving three gluons (such as the gluon self-coupling in QCD).

- **Gluon–top vertices:** the coupling between a gluon and a top–antitop pair (relevant, for example, in diagrams where a gluon splits into $t\bar{t}$ or when a gluon is emitted from a top quark).

- **Four-fermion vertices (2 top quarks + 2 light quarks):** effective interactions in which two initial-state light quarks and two final-state top quarks interact directly at a four-fermion vertex, without gluon exchange.

(a) purely gluonic interactions   (b) gluon–top couplings

(c) four-fermion contact interactions ($q\bar{q}t\bar{t}$)
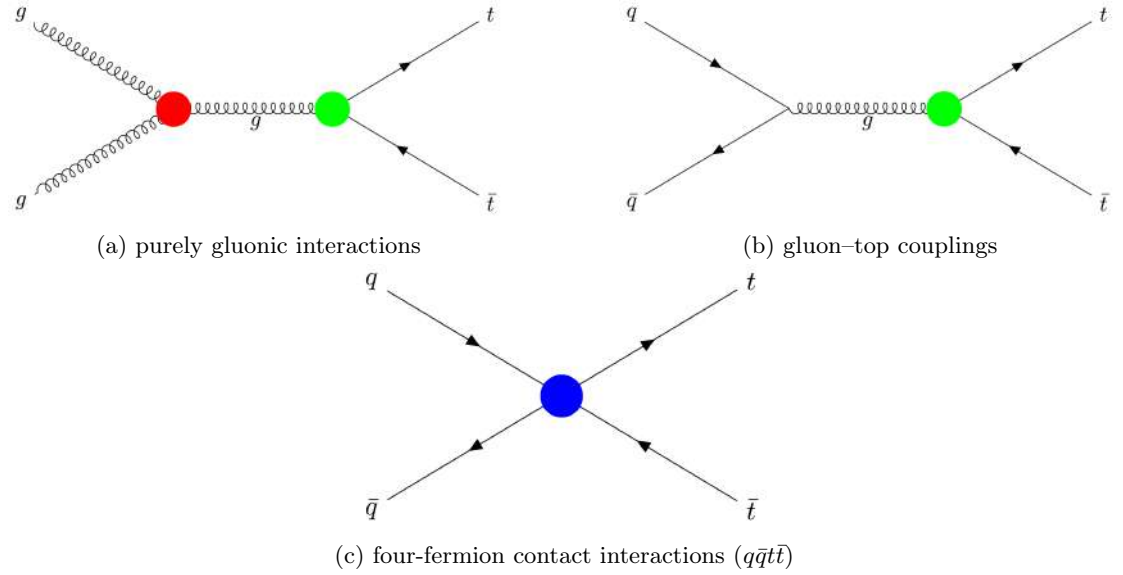
Figure 2.9: Representative SMEFT vertices contributing to top–antitop production at the LHC. The color code indicates: blue for four-fermion interactions, green for top–antitop–gluon couplings, and red for purely gluonic vertices.

These additional couplings are illustrated in Fig. 2.9, and the corresponding operators are presented below. The selection of operators for this work is motivated from Ref. [1] under the assumptions of baryon number conservation, CP invariance, and a flavor symmetry of the form $U(2)_Q \times U(2)_u \times U(3)_d$.

The relevant set of dimension-six operators includes:

- A two-fermion operator, the chromomagnetic dipole operator, modifying the top-gluon interaction (see Fig. 2.9 (b)):

$$\mathcal{O}_{tG} = g_s \, (\bar{Q} \, T^A \tilde{H} \sigma^{\mu\nu} \, t_R) \, G^A_{\mu\nu} \tag{2.45}$$

where the third generation quark doublet is denoted $Q = (t_L, b_L)^T$, $\tilde{H}$ is the conjugate Higgs doublet $\tilde{H} = i\sigma^2 H^*$, and $\sigma^{\mu\nu}$ is the antisymmetric combination of gamma matrices $\sigma^{\mu\nu} = \frac{i}{2}[\gamma^\mu, \gamma^\nu]$.

- Seven independent four-fermion operators involving two light quarks (u, d, c, s) and two top quarks, in color octet and singlet version (Fig. 2.9 (c)):

$$\mathcal{O}_{tu}^{(8)} = \sum_{f=1}^{2} (\bar{t}_R \gamma^\mu T^A t_R)(\bar{u}_f \gamma_\mu T^A u_f), \tag{2.46}$$

$$\mathcal{O}_{td}^{(8)} = \sum_{f=1}^{3} (\bar{t}_R \gamma^\mu T^A t_R)(\bar{d}_f \gamma_\mu T^A d_f), \tag{2.47}$$

$$\mathcal{O}_{tq}^{(8)} = \sum_{f=1}^{2} (\bar{q}_f \gamma^\mu T^A q_f)(\bar{t}_R \gamma_\mu T^A t_R), \tag{2.48}$$

$$\mathcal{O}_{Qu}^{(8)} = \sum_{f=1}^{2} (\bar{Q} \gamma^\mu T^A Q)(\bar{u}_f \gamma_\mu T^A u_f), \tag{2.49}$$

$$\mathcal{O}_{Qd}^{(8)} = \sum_{f=1}^{3} (\bar{Q} \gamma^\mu T^A Q)(\bar{d}_f \gamma_\mu T^A d_f), \tag{2.50}$$

$$\mathcal{O}_{Qq}^{(1,8)} = \sum_{f=1}^{2} (\bar{Q} \gamma^\mu T^A Q)(\bar{q}_f \gamma_\mu T^A q_f), \tag{2.51}$$

$$\mathcal{O}_{Qq}^{(3,8)} = \sum_{f=1}^{2} (\bar{Q} \gamma^\mu T^A \sigma^I Q)(\bar{q}_f \gamma_\mu T^A \sigma^I q_f), \tag{2.52}$$

where

- Q: SU(2)$_L$ doublet of the third generation,

$$Q = \begin{pmatrix} t_L \\ b_L \end{pmatrix}.$$

- q_f: SU(2)$_L$ doublet of the first or second generation,

$$q_f = \begin{pmatrix} u_{Lf} \\ d_{Lf} \end{pmatrix}, \qquad f = 1, 2.$$

- u_f: SU(2)$_L$ singlet for right-handed up-type light quarks,

$$u_f \in \{u_R, c_R\}, \qquad f = 1, 2.$$

- d_f: SU(2)$_L$ singlet for right-handed down-type quarks,

$$d_f \in \{d_R, s_R, b_R\}, \qquad f = 1, 2, 3.$$

- t_R: SU(2)$_L$ singlet for the right-handed top quark,

These four-fermion operators affect $t\bar{t}$ production mainly via quark-antiquark annihilation channels and play a central role in modifying angular distributions and spin correlations of the top quark pair.

3 Materials and Methods

3.1 Monte Carlo

Monte Carlo (MC) methods are a key component of the ATLAS simulation framework, as they enable the generation of theoretical particle collisions based on both SM and beyond-the-SM physics. These simulated datasets are used to study the detector response, optimize reconstruction algorithms, and compare theory with experiment, thus providing a means to search for new physics [33]. In ATLAS, event generators such as Pythia and POWHEG model high-energy proton-proton collisions through random sampling of quantum interactions, producing detailed information on particle energies and trajectories. The resulting events are then processed with Geant4, which simulates the passage of particles through the detector, recording energy deposits as *hits* that allow accurate modeling of the detector response and direct comparison with data [33].

In this work, the analysis is performed with events at generator level, i.e. before simulating the detector response. At this stage the information corresponds directly to the partons and particles produced in the collision, without including any distortions from the detector. This choice allows to test the sensitivity of the observables to SM and SMEFT effects in a clean environment.

Two MC samples produced by the ATLAS Collaboration were used in this work: one including SMEFT dimension-6 effects and one nominal sample. The first sample corresponds to a simulation of $pp \rightarrow t\bar{t}$ at leading order (LO) in QCD, generated with MadGraph5_aMC@NLO [34] and PYTHIA8 [35]. This sample was re-weighted using the SMEFTsim package [36], where the SM is extended with dimension–6 SMEFT operators.

The nominal dataset is a Monte Carlo simulation of top–antitop pair production at $\sqrt{s} = 13$ TeV, generated at next-to-leading order (NLO) in QCD with Powheg-Box [37] interfaced to Pythia8 for parton showering and hadronization. Only semileptonic and dileptonic decays are included, while fully hadronic top decays are excluded. This sample serves as the SM reference for $t\bar{t}$ production in the present analysis.

However, when comparing these results with real data measured by ATLAS and CMS, one must take into account the impact of the detector, which alters the distributions. The experimental collaborations correct their data for these detector effects using fully simulated samples. These samples are produced by passing the generated events through the complete chain of detector simulation, digitization, and event reconstruction, ensuring that the same reconstruction algorithms are applied as in real data. Only after this

correction can the MC predictions and the experimental distributions be consistently compared [33].

3.2 Analysis

This analysis was carried out at parton level, without reconstruction. The selection of events for the analysis is $t\bar{t}$ production in the single-lepton topology: exactly one charged lepton (e, μ) and one neutrino from a W decay, the other W decaying hadronically into two light quarks, together with the accompanying b and $\bar{b}$ from the top and antitop decays. dileptonic and fully hadronic topologies are are excluded from the analysis. No additional generator-level kinematic cuts are imposed beyond the parton-level object definitions, and QCD ISR/FSR is allowed. The quarks used for the observable reconstruction are selected after the radiation of gluons but prior the hadronization.

The produced ntuples with this configuration contain kinematic variables of the events, the polarization of the top and anti-top quarks in different reference frames (e.g. lab frame, helicity frame), as well as the projection of the spin along different axes (e.g. helicity, r-axis, transverse), as presented in Section 2.2.1. The purpose is to extract and study spin correlations C_{ij} and observables such as the entanglement marker D_3, the Bell inequality marker A^+, and the sum of weights $N_{\text{events}} = \sum w_{\text{EFT}}$, with the sum running over all events. The observable N_{events} corresponds to the expected number of events once multiplied by a normalization factor used to re-scale to the proper luminosity. In addition, the sensitivity of these observables to deviations induced by dimension-6 SMEFT operators in top-quark production is studied. The set of operators considered is summarized in Section 2.3.2.

Two kinematic variables play a central role in this analysis: the cosine of the angle between the top quark and the beam axis in the $t\bar{t}$ center-of-mass frame, $\cos\theta$, and the invariant mass of the system, $m_{t\bar{t}}$. Based on these variables, different kinematic regions are defined in order to enhance sensitivity to specific observables. The definition of different kinematic regions is obtained by applying cuts on these two observables. In this thesis, four regions are considered: Threshold, Boosted, Central Boosted, and Central High-Boosted, whose definitions are summarized in Table 3.1.

Table 3.1: Definition of the kinematic regions employed in the analysis. Each region is characterized by specific selections on the invariant mass of the $t\bar{t}$ system, $m_{t\bar{t}}$, and on the scattering angle, $\cos\theta$.

Region	Cut Applied
Threshold	$m_{t\bar{t}} < 400$ GeV
Boosted	$m_{t\bar{t}} > 800$ GeV
Central Boosted	$m_{t\bar{t}} > 800$ GeV, $\lvert\cos\theta\rvert < 0.4$
Central Highly-Boosted	$m_{t\bar{t}} > 1500$ GeV, $\lvert\cos\theta\rvert < 0.2$

These regions are selected because they probe complementary parts of the phase space, maximizing the sensitivity to spin–correlation observables and to different SMEFT operators, from entanglement near threshold to energy-enhanced effects in the boosted regime.

The helicity basis, discussed in Section 2.2.1, is adopted throughout this analysis, as it provides optimal sensitivity to spin correlations and quantum observables. As spin analysers, the charged lepton and the down-type quark from the hadronic W decay are employed. This choice corresponds to the ideal case of maximal spin analysing power $\alpha = \pm 1$.

In order to reconstruct the spin-correlation coefficients C_{ij} in the helicity basis, it is first necessary to build the differential distribution of the product of the decay angles of the top and anti-top spin analyzers, namely $\cos\theta_i^+ \cos\theta_j^-$, with $i, j = k, r, n$. These angles are separately reconstructed and available in the ntuple. The corresponding histograms were constructed and subsequently normalized, and then used to extract the spin–correlation coefficients according to Eq. 2.34. The normalization does not affect the values of the spin–correlations, since they are obtained as the mean value of the histograms.

The construction of the histograms was carried out separately for each of the four distinct kinematic regions mentioned above. After establishing the general method and for further baseline comparison, the differential distributions for the diagonal case C_{ii} were constructed using the nominal sample for each kinematic region. The distributions for the boosted and central highly-boosted regions are shown in Figure 3.1. The numerical values of C_{kk}, C_{rr}, and C_{nn} are indicated in the corresponding figures. Using these numerical values, it is possible to calculate the Bell–violation indicator A^+ according to Eq. 2.42.

In order to calculate the entanglement marker D_3, the distribution of the kinematic variable $\cos\theta'_{ab}$ needs to be built, following Eq. 2.38. The construction of this distribution, as well as that of $\cos\theta_k^+ \cos\theta_r^-$, are shown in Figure 3.2 for the boosted and central highly-boosted regions, together with the corresponding values of D_3 and C_{kr}.

The observables calculated at NLO QCD using the nominal sample are summarized in Tables 3.2 and 3.3 for the four kinematic regions considered, extracted from the distributions.

Table 3.2: Diagonal spin–correlation observables C_{kk}, C_{rr} and C_{nn} in the four kinematic regions calculated at NLO QCD. Uncertainties are statistical.

Region	C_{kk}	C_{rr}	C_{nn}
Threshold	$+0.505 \pm 0.004$	$+0.291 \pm 0.004$	$+0.486 \pm 0.004$
Boosted	-0.056 ± 0.007	-0.125 ± 0.007	$+0.177 \pm 0.007$
Central Boosted	-0.482 ± 0.025	-0.656 ± 0.024	$+0.563 \pm 0.024$
Central Highly-Boosted	-0.810 ± 0.240	-1.484 ± 0.206	$+0.465 \pm 0.204$

(a) Central highly-boosted region.
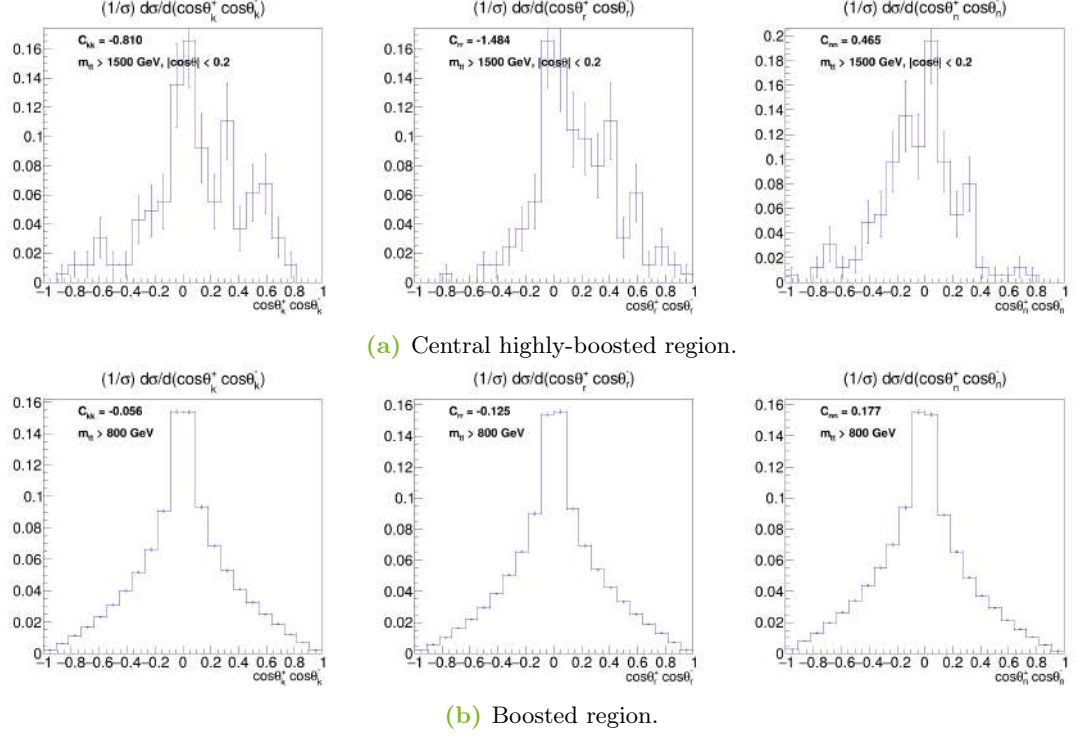
(b) Boosted region.
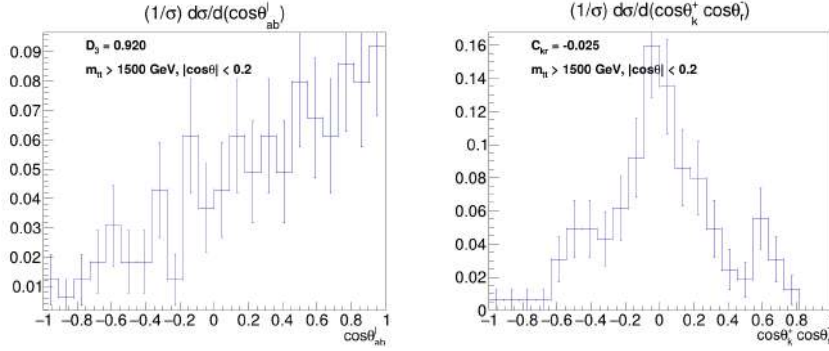
Figure 3.1: Normalized distributions used to extract the spin–correlation coefficients C_{kk}, C_{rr}, C_{nn}, and the asymmetry A^+ in the boosted and central high-boosted regions of $t\bar{t}$ production at NLO in QCD.
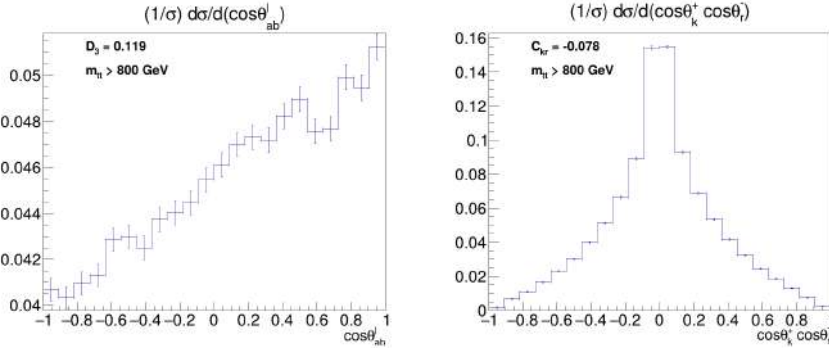
Table 3.3: Mixed spin–correlation observable C_{kr}, the observable D_3, and the azimuthal asymmetry A^+ in the four kinematic regions calculated at NLO QCD. Uncertainties are statistical.

Region	C_{kr}	D_3	A^+
Threshold	-0.080 ± 0.004	-0.103 ± 0.002	-0.156 ± 0.001
Boosted	-0.078 ± 0.007	$+0.119 \pm 0.004$	$+0.036 \pm 0.002$
Central Boosted	-0.105 ± 0.025	$+0.567 \pm 0.014$	$+0.223 \pm 0.007$
Central Highly-Boosted	-0.025 ± 0.243	$+0.920 \pm 0.117$	$+0.450 \pm 0.059$

(a) Central highly-boosted region.

(b) Boosted region.

Figure 3.2: Normalized distributions used to extract the mixed spin–correlation coefficient C_{kr} and the angular observable D_3 in the boosted and central highly-boosted regions of $t\bar{t}$ production at NLO in QCD.

From Figures 3.1 and 3.2, together with Tables 3.2 and 3.3, it can be seen that all distributions exhibit peaked shapes around zero, with the exception of the angle entering D_3, which is linear. When comparing the different kinematic regions, the absolute values of all spin-correlation coefficients increase when moving to the central boosted regions. However, the statistics are very limited for the central high-boosted region.

In particular, D_3 exhibits a pronounced enhancement in the central boosted region and exceeds the critical value $1/3$ starting from this regime, indicating that it is where entanglement in the $t\bar{t}$ system starts to become observable. The azimuthal asymmetry A^+ follows a similar trend, albeit with a less pronounced effect.

For the spin-correlations in the threshold region, the diagonal coefficients C_{kk}, C_{rr}, and C_{nn} are positive. As the invariant mass increases, the correlations C_{kk} and C_{rr} weaken and eventually flip sign, becoming strongly negative in the central boosted and central high-boosted regimes. The coefficient C_{nn}, in contrast, shows little variation across the threshold, central boosted, and central high-boosted regimes, and remains positive in all

cases. The mixed term C_{kr} is consistently negative and small across all regions, with only minor variations.

In Section 4.3, these observables are compared with the corresponding CMS results, and the impact of dimension-6 SMEFT operators is investigated. Their effects and sensitivities are systematically analyzed across different regions introduced in this section.

3.3 Impact of Relevant Operators

As previously mentioned, this study focuses on dimension-6 operators that affect top-quark pair production, modifying the $\cos\theta_i^+ \cos\theta_j^-$ distributions and, consequently, the spin correlations and quantum observables. Having established the procedure for extracting these distributions and calculating the observables, the next step is to quantify the deviations from the SM predictions induced by such operators.

For this purpose, the SMEFT reweighted sample is employed. This sample provides multiple event weights that account for the effects of different dimension-6 SMEFT operators on $t\bar{t}$ production, introduced in Section 2.3.2. A distribution filled with a given weight therefore represents the distribution that would be observed if the interaction associated with that operator were present in nature.

In practice, both single-operator weights and two-operator weights are provided. The former isolate the contribution of an individual operator, while the latter account for the combined effect of pairs of operators, including possible interference terms. This allows to study systematically both effects separately.

3.3.1 Single Operator Effects

In order to study the impact of SMEFT contributions on $t\bar{t}$ production, the effect of each operator is first considered individually. Each operator is accompanied by a WCs, as shown in Eq. 2.43. In the sample, every WCs is evaluated at four benchmark values, each encoded as a separate event weight. This setup makes it possible to construct distributions reflecting the presence of a given operator and to directly compare them to the SM expectation. The set of operators relevant for $t\bar{t}$ production included in the sample and employed in this analysis, together with the corresponding weight names associated with their WCs, is listed below:

Chromomagnetic dipole operator

$$\mathcal{O}_{tG}$$

Associated with the real and imaginary parts of its WCs, $\mathrm{Re}(c_{tG})$ and $\mathrm{Im}(c_{tG})$, corresponding to the weight labels `tGRe` and `tGIm`.

Four-fermion operators (color singlet)

$$\mathcal{O}_{td}^{(1)}, \quad \mathcal{O}_{tu}^{(1)}, \quad \mathcal{O}_{tj}^{(1)}, \quad \mathcal{O}_{Qu}^{(1)}, \quad \mathcal{O}_{Qd}^{(1)}, \quad \mathcal{O}_{Qj}^{(1,1)}, \quad \mathcal{O}_{Qj}^{(3,1)}$$

With corresponding weights: `td1`, `tu1`, `tj1`, `Qu1`, `Qd1`, `Qj11`, `Qj31`.

Four-fermion operators (color octet)

$$\mathcal{O}_{td}^{(8)}, \quad \mathcal{O}_{tu}^{(8)}, \quad \mathcal{O}_{tj}^{(8)}, \quad \mathcal{O}_{Qu}^{(8)}, \quad \mathcal{O}_{Qd}^{(8)}, \quad \mathcal{O}_{Qj}^{(1,8)}, \quad \mathcal{O}_{Qj}^{(3,8)}$$

Analogous to the color–singlet case, but in the color–octet representation, with weights: `td8`, `tu8`, `tj8`, `Qu8`, `Qd8`, `Qj18`, `Qj38`.

The available benchmark values of the WCs are provided within predefined ranges. These ranges determine the parameter space that can be explored in this analysis and are motivated by the existing limits on these operators. Figure 3.3 shows the scan ranges considered for each operator: the horizontal lines indicate the full allowed ranges, while the red points correspond to the specific benchmark values available in the sample.
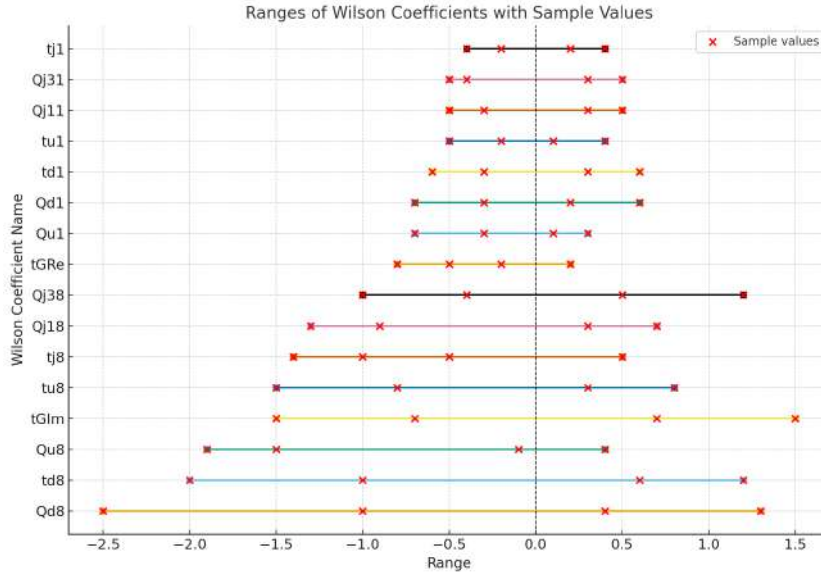

Figure 3.3: Ranges of Wilson coefficients considered in the analysis. Horizontal lines indicate the allowed scan ranges, while red points correspond to the benchmark values available in the sample.

To assess the impact of each individual operator, the differential distributions defined in Eqs. 2.32 were constructed for all one-operator weights for the available benchmark values of their WCs. By comparing these SMEFT-weighted distributions to the SM-weighted distribution, also provided in the sample, the modifications induced by the operators can be quantified.

The comparison with the SM reference demonstrates that all operator weights lead to explicit modifications of the angular distributions, with the size of the effect depending

on the benchmark value of the corresponding WC. The distortions shown in Figs. 3.4, obtained using the largest available benchmark values, provide a clear visualization of these effects. In the subsequent analysis, the full set of benchmark weights is employed to systematically quantify the deviations in the spin–correlation coefficients and related observables, as well as their parametric dependence on the WCs.
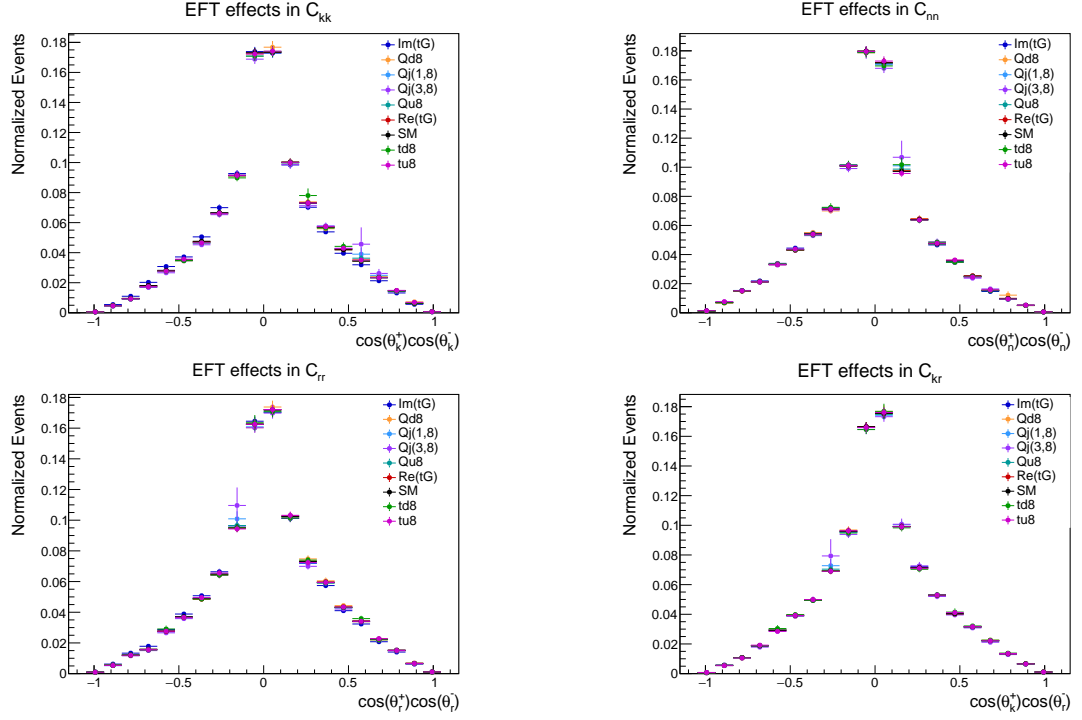
Figure 3.4: Effects of different dimension-6 SMEFT operators on the differential cross section.

Parametrization of EFT Effects for Single Operators

From the weighted histograms, the following observables were extracted: N_{events}, C_{kk}, C_{rr}, C_{nn}, C_{kr}, D_3, and A^+. For each single operator listed, the ratio between the SMEFT prediction O_{EFT} and the SM prediction O_{SM} was computed. To describe the dependence of the observables on the WCs, polynomial fits were performed, providing a systematic framework to assess their sensitivity to new physics.

In the case of a single operator, the EFT prediction for an observable O_{EFT} is modeled as a quadratic polynomial function of the corresponding WC c, of the form:

$$O_{EFT}(c) = \alpha_0 + \alpha_1 \, c + \alpha_2 \, c^2, \tag{3.1}$$

where α_i are real coefficients encoding the parametric dependence of the observable on c. The parametrization in Eq. 3.1 captures at LO the full dependence expected from the SMEFT expansion. Specifically, α_0 corresponds to the SM prediction, α_1 encodes the linear interference between the SM amplitude and the dimension-6 operator, and α_2 represents the pure quadratic contribution of the dimension-6 operator.

The truncation at order c^2/Λ^4 is consistent with the EFT expansion at dimension-6, since higher-order terms in c would correspond either to dimension-8 operators or to multiple insertions of dimension-6 operators, neither of which are included in this analysis. It should be noted, however, that the quadratic term α_2 may in principle also contain contributions from the interference between dimension-6 and dimension-8 operators. Such effects are beyond the scope of the present study and are therefore neglected.

The coefficients α_i were determined from these fits, providing an interpolation that allows the prediction of the observable for arbitrary values of c within the scan range. The resulting functions, normalized to O_{SM}, are illustrated in Figure 4.2 (boosted region) and Figure 4.1 (threshold region), for different operators.

To investigate which operator leads to the largest deviation from the SM prediction, each observable was evaluated using the polynomial parametrization obtained previously. For every observable in each kinematic region, a dedicated figure was produced containing multiple fitted curves. Each curve corresponds to the polynomial fit of the observable as a function of a single operator, obtained from the EFT samples with all other operators set to zero. This representation allows for a direct comparison of the effects of different operators. The results are shown in Figure 4.3 for the threshold region and Figure 4.4 for the central boosted region.

Building on these results, the sensitivity of all operators was then quantified in terms of the relative deviation of each observable with respect to the SM prediction. This provides a direct measure of which operators induce the largest modifications in the spin–correlation coefficients and quantum observables. The outcome of this comparison is summarized in Table 4.1.

3.3.2 Double Operator Effects

While the analysis of single operators provides valuable insight into their individual impact, SMEFT corrections in realistic scenarios typically involve simultaneous contributions from multiple operators. Interference effects between operator pairs can induce non-trivial modifications of observables, leading to either enhancements or suppressions relative to the single-operator case. To capture these effects, the analysis is extended to event weights corresponding to two-operator insertions, which are included in the SMEFT sample and enable the study of combined contributions.

For each operator pair, the sample provides four distinct weights corresponding to different values of the associated WCs. All pairwise combinations of the following nine operators are included in the sample and are considered in this analysis:

$$\{\mathcal{O}_{tG}, \mathcal{O}_{td}^{(8)}, \mathcal{O}_{tu}^{(8)}, \mathcal{O}_{tj}^{(8)}, \mathcal{O}_{Qu}^{(8)}, \mathcal{O}_{Qd}^{(8)}, \mathcal{O}_{Qj}^{(1,8)}, \mathcal{O}_{Qj}^{(3,8)}, \mathcal{O}_{Qj}^{(3,1)}\}.$$

In the above combinations, only the real part of the WC associated with $\mathcal{O}_{tG}$ is available, named in the sample as `tGRe`. And the only color-singlet four-fermion operator included is $\mathcal{O}_{Qj}^{(3,1)}$.

For each operator pair, a total of 12 sampling points (c_1, c_2) in the space of WCs can be extracted from the sample, together with the Standard Model point $(0, 0)$. These consist of four variations for each operator individually, $(c_1, 0)$ or $(0, c_2)$ (already discussed in the previous section), and four cross-points where both (c_1, c_2) take non-zero values. This sampling is sufficient to fully constrain the quadratic dependence of observables on the WCs. The discrete scan values for each operator are shown in Table 3.4, and the corresponding ranges are consistent with those displayed in Figure 3.3.

Wilson Coeff.	Range	Discrete values
`tGRe`	$[-0.8, 0.2]$	$-0.8, -0.5, -0.2, 0.2$
`td8`	$[-2.0, 1.2]$	$-2.0, -1.0, 0.6, 1.2$
`tu8`	$[-1.5, 0.8]$	$-1.5, -0.8, 0.3, 0.8$
`tj8`	$[-1.4, 0.5]$	$-1.4, -1.0, -0.5, 0.5$
`Qu8`	$[-1.9, 0.4]$	$-1.9, -1.5, -0.1, 0.4$
`Qd8`	$[-2.5, 1.3]$	$-2.5, -1.0, 0.4, 1.3$
`Qj18`	$[-1.3, 0.7]$	$-1.3, -0.9, 0.3, 0.7$
`Qj31`	$[-0.5, 0.5]$	$-0.5, -0.4, 0.3, 0.5$
`Qj38`	$[-1.0, 1.2]$	$-1.0, -0.4, 0.5, 1.2$

Table 3.4: Wilson coefficient scan values for each dimension-six operator. Ranges are shown together with the discrete values actually generated in the sample.

The observables N_{events}, C_{kk}, C_{rr}, C_{nn}, D_3, A^+ were evaluated for each operator pair listed above in the threshold, boosted, central boosted, and central high-boosted regions at LO QCD. In addition, the corresponding SM predictions were computed. All results were stored for each case to enable subsequent analysis.

Parametrization of EFT Effects for Pair of Operators

Similar to the one-operator effect presented in Section 3.3.1, polynomial fits were employed to model the dependence of observables, in this case as a function of two WCs c_1 and c_2 corresponding to different operators. The dependence of each observable is given as a quadratic polynomial of the form

$$O_{\text{EFT}}(c_1, c_2) = \alpha_1 + \alpha_2 c_1 + \alpha_3 c_2 + \alpha_4 c_1^2 + \alpha_5 c_2^2 + \alpha_6 c_1 c_2. \qquad (3.2)$$

The two-parameter expansion in Eq. 3.2 captures, at leading order, the following structure: the SM baseline is encoded in α_1; the linear SM–EFT interference terms along the two Wilson directions are described by $\alpha_2 c_1$ and $\alpha_3 c_2$; the purely quadratic SMEFT contributions are given by $\alpha_4 c_1^2$ and $\alpha_5 c_2^2$; and the mixed quadratic term $\alpha_6 c_1 c_2$ accounts for the interference between the two operators.

The coefficients α_i were determined from these surface fits, providing an interpolation that allows the prediction of the observable for arbitrary values of c_1 and c_2 within the scan range. The resulting surface functions, normalized to O_{SM}, are displayed in Figure 3.5 for the operator pair $(\mathcal{O}_{Qj}^{(3,1)}, \mathcal{O}_{td}^{(8)})$, and in Figure 3.6 for the pair $(\mathcal{O}_{Qj}^{(1,8)}, \mathcal{O}_{Qu}^{(8)})$, both evaluated in the central boosted region.
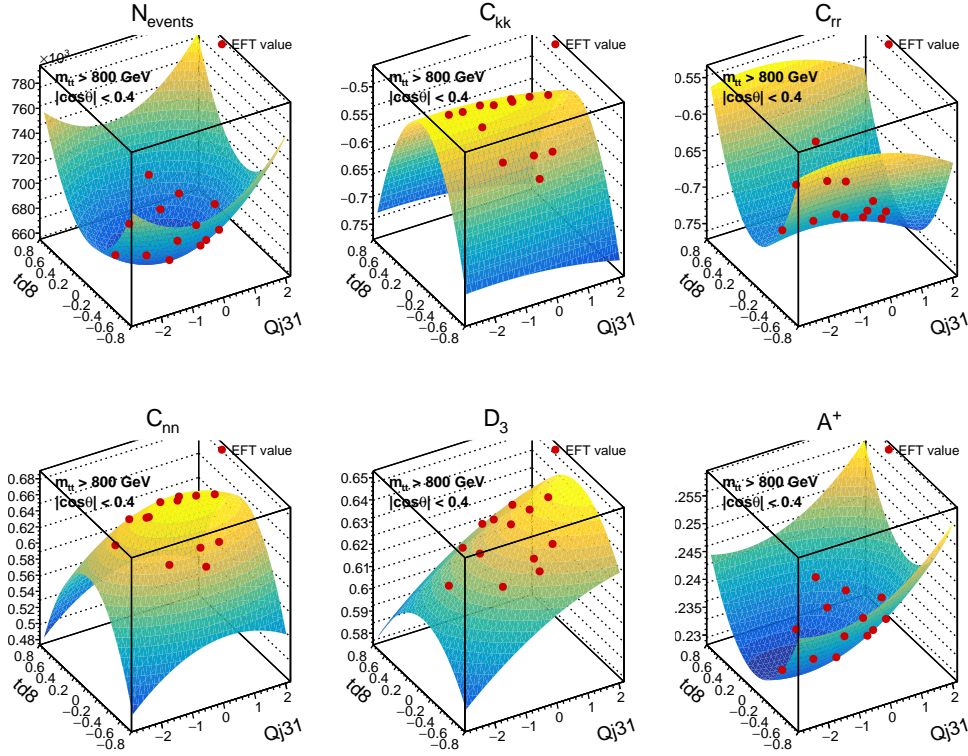
Figure 3.5: Dependence of O_{EFT}/O_{SM} on the WCs for the operator pair $(\mathcal{O}_{Qj}^{(3,1)}, \mathcal{O}_{td}^{(8)})$ in the central boosted regime. Each panel shows a different observable (N_{events}, C_{kk}, C_{rr}, C_{nn}, D_3, A^+), normalized to the SM. A quadratic surface fit in (c_1, c_2) is overlaid.
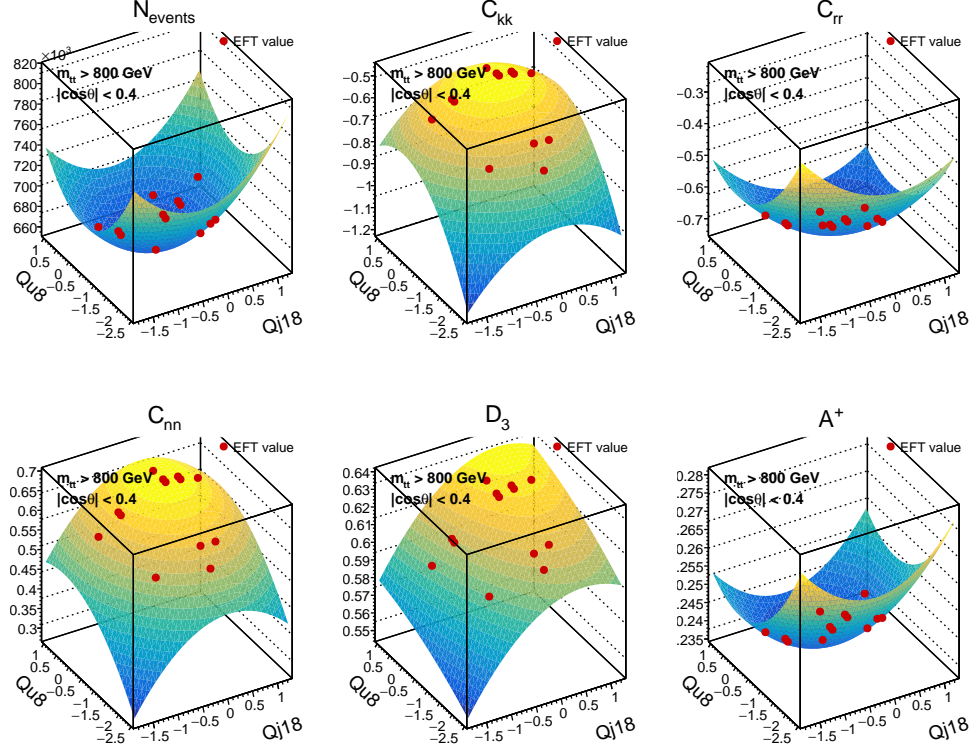
Figure 3.6: Dependence of O_{EFT}/O_{SM} on the WCs for the operator pair $(\mathcal{O}_{Qj}^{(1,8)}, \mathcal{O}_{Qu}^{(8)})$ in the central boosted regime. Each panel shows a different observable (N_{events}, C_{kk}, C_{rr}, C_{nn}, D_3, A^+), normalized to the SM. A quadratic surface fit in (c_1, c_2) is overlaid.

As shown, the response of each physics observable is characterized under variations of the WCs , and depending on the kinematic region, the influence of a given operator can be predominantly linear or quadratic. A linear dependence indicates a dominant contribution from the interference between the SM and the dimension-6 operator, whereas a quadratic dependence reflects dominance of the pure operator contribution. In particular, the quadratic dependence is found to dominate in the boosted regions.

In the case of the two-operator parametrization, the resulting surfaces in the boosted and central boosted regimes exhibit positive-parabolic, negative-parabolic, or saddle-like shapes. The dependence of O_{EFT}/O_{SM} on pairs of WC was explored in composite figures. Each figure contained the observables N_{events}, C_{kk}, C_{rr}, C_{nn}, D_3, and A^+, together with quadratic surface fits in the (c_1, c_2) parameter space.

The extracted coefficients α_i from the one- and two-dimensional fits of each observable in all four kinematic regions are stored for further processing. These coefficients

enable sensitivity estimates and uncertainty propagation without the need for additional simulations, providing a compact input for subsequent parameter estimation or limit setting.

3.4 EFT Fitter

The interpretation of measurements within the EFT framework requires a statistical method capable of constraining the WCs of higher-dimensional operators. In this analysis, the `EFTfitter` tool [38] is employed. It provides a Bayesian framework that combines predictions with experimental measurements in order to extract posterior probability distributions for the parameters of interest, determine credible intervals for EFT coefficients, and assess the relative constraining power of different observables.

The implementation of `EFTfitter` relies on the Bayesian Analysis Toolkit (BAT) and performs the fit using Markov Chain Monte Carlo (MCMC) sampling, which enables marginalization over nuisance parameters and the computation of credible intervals. The method is based on Bayes' theorem, which relates the posterior probability distribution $p(\boldsymbol{\lambda}|\boldsymbol{x})$ of the model parameters $\boldsymbol{\lambda}$ given the data $\boldsymbol{x}$ to the likelihood $\mathcal{L}(\boldsymbol{x}|\boldsymbol{\lambda})$ and the prior distribution $\pi(\boldsymbol{\lambda})$ through

$$p(\boldsymbol{\lambda}|\boldsymbol{x}) = \frac{\mathcal{L}(\boldsymbol{x}|\boldsymbol{\lambda})\,\pi(\boldsymbol{\lambda})}{p(\boldsymbol{x})}, \tag{3.3}$$

where $p(\boldsymbol{x})$ is the evidence, which acts as a normalization factor in Bayesian inference.

In practice, the parameters $\boldsymbol{\lambda}$ are not directly observable. Instead, a set of measurable quantities y_i is considered, each of which depends on the underlying parameters, i.e. $y_i = y_i(\boldsymbol{\lambda})$.

3.4.1 Modeling the SMEFT Effects in Observables

In order to perform an EFT interpretation, the following ingredients are required:

1. Theoretical predictions for the observables of interest, O_{EFT}, expressed as functions of the parameters to be constrained.

2. Experimental measurements of these observables, O^{meas}.

3. The set of model parameters to be constrained, in the case of this work, the Wilson coefficients.

Observables

The observables under consideration must be sensitive to EFT effects. In this analysis, the quantities of interest are those already discussed throughout this work, namely: N_{events},

C_{kk}, C_{rr}, C_{nn}, C_{kr}, D_3, and A^+. As shown in Section 3.3.1, these observables exhibit enhanced sensitivity to EFT contributions in the boosted region.

The expected EFT contributions to the i-th observable are parameterized in terms of two WCs corresponding to two distinct dimension-6 operators, as explained in Section 3.3.2:

$$y_i(c_1, c_2) = \alpha_{0,i} + \alpha_{1,i}\, c_1 + \alpha_{2,i}\, c_1^2 + \alpha_{3,i}\, c_2 + \alpha_{4,i}\, c_2^2 + \alpha_{5,i}\, c_1 c_2, \tag{3.4}$$

where $\alpha_{j,i}$ $(j = 0, 1, \ldots, 5)$ are the polynomial coefficients obtained from fits, for each observable $i = 1, 2, \ldots, 7$ in the vector

$$\boldsymbol{y} = \big(N_{\text{events}},\, C_{kk},\, C_{rr},\, C_{nn},\, C_{kr},\, D_3,\, A^+\big). \tag{3.5}$$

The functional dependence of the observables on the WCs is given by the quadratic parametrisation derived in the previous Section 3.3.1 and Section 3.3.2, with coefficients $\alpha_{j,i}$ obtained from the fits described there.

Measurements

The measurements of the observables of interest correspond to the SM predictions at leading order in QCD, denoted as O_{SM}^{LO}, and extracted from the SMEFT simulation sample used in this analysis. The measurement vector is defined as

$$\boldsymbol{m}_{LO} = \big(N_{\text{events}}^{SM},\, C_{kk}^{SM},\, C_{rr}^{SM},\, C_{nn}^{SM},\, C_{kr}^{SM},\, D_3^{SM},\, A^{+,SM}\big). \tag{3.6}$$

Statistical uncertainties were sample and added to the individual measurement values. No correlations between different observables were assumed, such that the covariance matrix is taken as diagonal.

Since the parameters of interest, $\boldsymbol{\lambda}$, in this case the WCs, are not directly observable, the likelihood is constructed from the predicted observables $\boldsymbol{y}(\boldsymbol{\lambda})$ that depend functionally on them. The `EFTfitter` tool is then used to perform the fit by minimizing the log-likelihood under the Gaussian approximation:

$$-2\ln \mathcal{L}(\boldsymbol{m}_{LO}|\boldsymbol{\lambda}) = \big(\boldsymbol{m}_{LO} - \boldsymbol{y}(\boldsymbol{\lambda})\big)^{\mathrm{T}} \mathbf{M}^{-1} \big(\boldsymbol{m}_{LO} - \boldsymbol{y}(\boldsymbol{\lambda})\big). \tag{3.7}$$

where $\mathbf{M}$ denotes the covariance matrix. In the present `EFTfitter` setup, a uniform 10% relative systematic uncertainty is assigned to the measurements in addition to the statistical uncertainties, while theoretical predictions are considered error-free and the measurements are treated as uncorrelated.

Parameters

The parameters of interest in the present EFT interpretation are the WCs associated with dimension-6 operators in the SMEFT framework. These coefficients encapsulate

the potential effects of new physics at an energy scale Λ beyond the SM and enter the predictions of the observables through polynomial dependencies, as described in the previous section. Since the fit is performed in the space of these coefficients, a proper definition of their allowed ranges and prior distributions is required in order to construct the Bayesian inference procedure. In this work, a uniform prior distribution is assigned to each WCs within its available range. The ranges differ from operator to operator and are extracted from the SMEFT sample, as summarized in Table 3.4.

To assess the relative impact of the different observables on the extracted posterior distributions and the ability of simultaneously constraining WCs, the fits were carried out under three complementary configurations:

1. Including the full set of observables,

2. Restricting the fit to N_{events} only,

3. Including all observables except for N_{events}.

This procedure enables a direct comparison between the constraining power of the global fit and that of individual observables. An example of this procedure is presented in the next section for the operators $\mathcal{O}_{Qj}^{(3,8)}$ and $\mathcal{O}_{Qj}^{(3,1)}$.

3.4.2 Example: Fit of C_{Qj38} and C_{Qj31}

As an illustration of the methodology, two operator weights are considered: `Qj38` and `Qj31`, with associated WCs C_{Qj38} and C_{Qj31}. The set of observables is chosen as

$$\boldsymbol{y} = \left(N_{\text{events}}, \, C_{kk}, \, C_{rr}, \, C_{nn}, \, C_{kr}, \, D_3, \, A^+ \right). \tag{3.8}$$

Possible systematic effects are introduced as nuisance parameters, varied within the range $[-1, 1]$. The predicted value of the i-th observable is expressed as a quadratic function of the WCs,

$$y_i(C_{Qj38}, C_{Qj31}) = \alpha_{0,i} + \alpha_{1,i} \, C_{Qj38} + \alpha_{2,i} \, C_{Qj38}^2 + \alpha_{3,i} \, C_{Qj31} + \alpha_{4,i} \, C_{Qj31}^2 + \alpha_{5,i} \, C_{Qj38} \, C_{Qj31}, \tag{3.9}$$

with coefficients $\alpha_{j,i}$ extracted from polynomial fits. The term $\alpha_{0,i}$ corresponds to the SM expectation, while the higher-order terms represent the EFT contributions.

The likelihood is modeled in `EFTfitter` as a multivariate Gaussian, constructed from the predicted observables $\boldsymbol{y}(C_{Qj38}, C_{Qj31})$, the reference values $\boldsymbol{m}_{LO}$, and the covariance matrix $\mathbf{M}$. In this analysis, $\mathbf{M}$ is taken as a 7×7 diagonal matrix, with a 10% experimental uncertainty assigned to each observable and correlations neglected. While this represents a simplified treatment, it is sufficient for the illustrative purpose of quantifying the interplay between C_{Qj38} and C_{Qj31}.

Flat priors are imposed according to the available ranges, in this case

$$p(C_{Qj38}) = \text{Uniform}(-1.0,\ 1.2), \qquad p(C_{Qj31}) = \text{Uniform}(-0.5,\ 0.5). \tag{3.10}$$

The posterior probability density is obtained internally by `EFTfitter` from the specified likelihood and priors. For illustration, the boosted region is presented: the marginalized posterior distributions for each WCs are shown in Figure 4.7, the corresponding credible intervals are summarized in Figure 4.10, and the relative constraining power of the different observables is quantified through a ranking analysis in Figure 4.5. The same set of results is provided for the central high-boosted region in Figures 4.9, 4.12, and 4.5b.

The procedure described in this example was repeated for all pairs of operators available in the SMEFT sample. For each case, the corresponding posterior distributions, credible intervals in the two-dimensional parameter space, and ranking of observables were obtained following the same methodology.

3.5 Comparison with CMS

To validate the results obtained in this thesis, a supplementary analysis was performed using the nominal sample. The spin–correlation coefficients C_{kk}, C_{rr}, and C_{nn} were calculated for SM $t\bar{t}$ production at NLO in QCD, and the results were compared with the data reported by the CMS Collaboration [39].

The CMS analysis provides results in the following kinematic regions:

- $300 < m_{t\bar{t}} < 400$ GeV,

- $400 < m_{t\bar{t}} < 600$ GeV,

- $600 < m_{t\bar{t}} < 800$ GeV,

- $m_{t\bar{t}} > 800$ GeV,

both with and without the additional requirement $|\cos\theta| < 0.4$.

The values of the C_{kk}, C_{nn} and C_{rr} extracted from [39] are shown in Table 3.5. The comparisons are presented in Fig. 3.7 (without the angular cut) and Fig. 3.8 (with the angular cut).

Within the quoted uncertainties, the values obtained in this analysis are in good agreement with the measurements reported by CMS across all kinematic regions, both with and without the $|\cos\theta| < 0.4$ requirement. This consistency validates the implementation and confirms that the methodology adopted in this thesis reproduces the expected SM spin–correlation pattern at NLO in QCD.
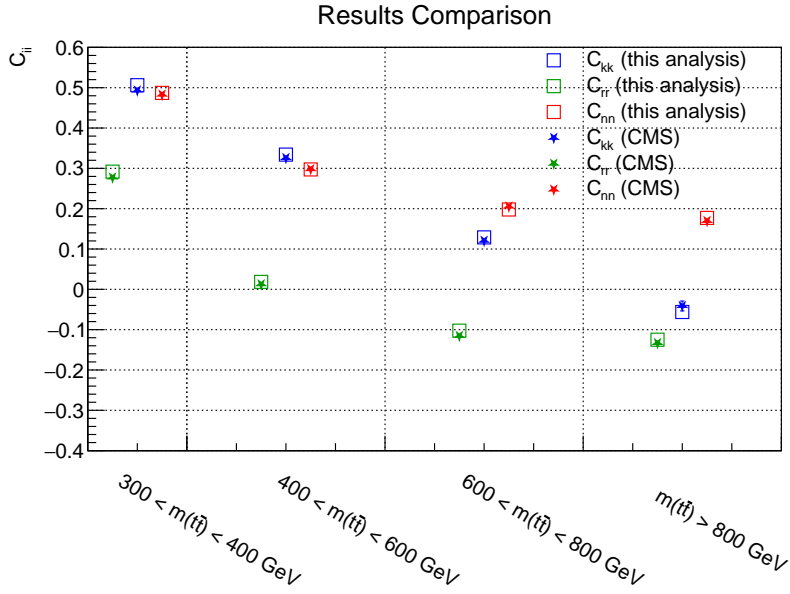
Figure 3.7: Comparison of the analysis results with CMS data for the diagonal spin-correlation coefficients in the helicity basis, without the angular cut.
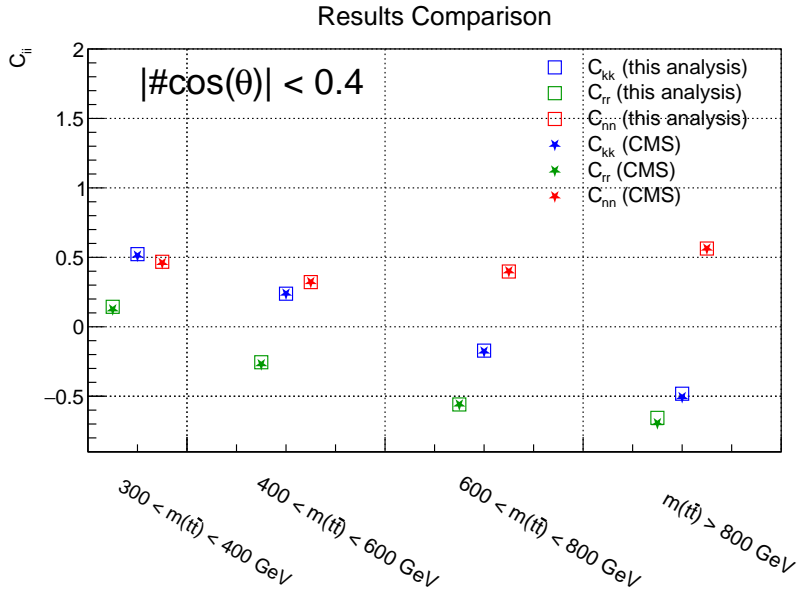
Figure 3.8: Comparison of the analysis results with CMS data for the diagonal spin-correlation coefficients in the helicity basis, with the angular cut $|\cos\theta| < 0.4$.

Table 3.5: Spin–correlation coefficients in $t\bar{t}$ production at high invariant mass reported by CMS [39]. Numerical values are extracted from the publication for comparison with the results of this analysis.

Observable	$m_{t\bar{t}} > 800\,\text{GeV}$	$m_{t\bar{t}} > 800\,\text{GeV},\ |\cos\theta| < 0.4$
C_{rr}	-0.1331 ± 0.0080	-0.6941 ± 0.0059
C_{nn}	0.1697 ± 0.0046	0.5630 ± 0.0042
C_{kk}	-0.0412 ± 0.0122	-0.5061 ± 0.0042

3.5.1 LO and NLO SM simulation

The dependence of the spin–correlations and quantum observables on the WCs has been investigated at LO QCD in Sections 3.3.1–3.3.2. However, the inclusion of the NLO description is essential for estimating the limits on the different WCs presented in this work, as the differences with LO are non-negligible when compared to data, and using LO fits would lead to biased constraints.

To consistently incorporate the SM prediction at NLO into this analysis, all fitted curves were re-scaled by the ratio of the SM results at NLO and LO. In the case of single-operator effects, this is achieved through:

$$O_{\text{corrected}}(c) = \frac{O_{\text{SM}}^{\text{NLO}}}{O_{\text{SM}}^{\text{LO}}} \left(\alpha_0 + \alpha_1 c + \alpha_2 c^2 \right). \tag{3.11}$$

This correction ensures consistency with the updated SM normalization while preserving the EFT dependence. Representative examples in the boosted region are shown in Figures 3.9-3.10.

In the case of two-operator effects, the EFT predictions were parameterized as functions of two WCs and fitted with a quadratic surface. The correction applied to the observables takes the form

$$O_{\text{corrected}}(c_1, c_2) = \frac{O_{\text{SM}}^{\text{NLO}}}{O_{\text{SM}}^{\text{LO}}} \left(\alpha_0 + \alpha_1 c_1 + \alpha_2 c_2 + \alpha_3 c_1^2 + \alpha_4 c_2^2 + \alpha_5 c_1 c_2 \right), \tag{3.12}$$

where the polynomial coefficients are obtained from fits. As in the single-operator case, the re-scaling by the NLO-to-LO SM ratio ensures consistency with the SM normalization while preserving the EFT dependence.
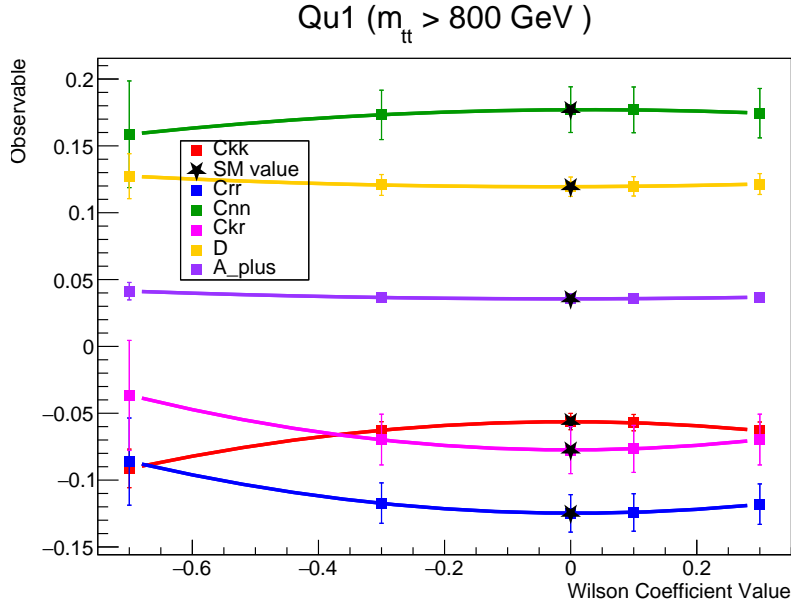
Figure 3.9: One-operator scan for Q_{u1} in the boosted region ($m_{t\bar{t}} > 800$ GeV). The SM reference point is indicated.
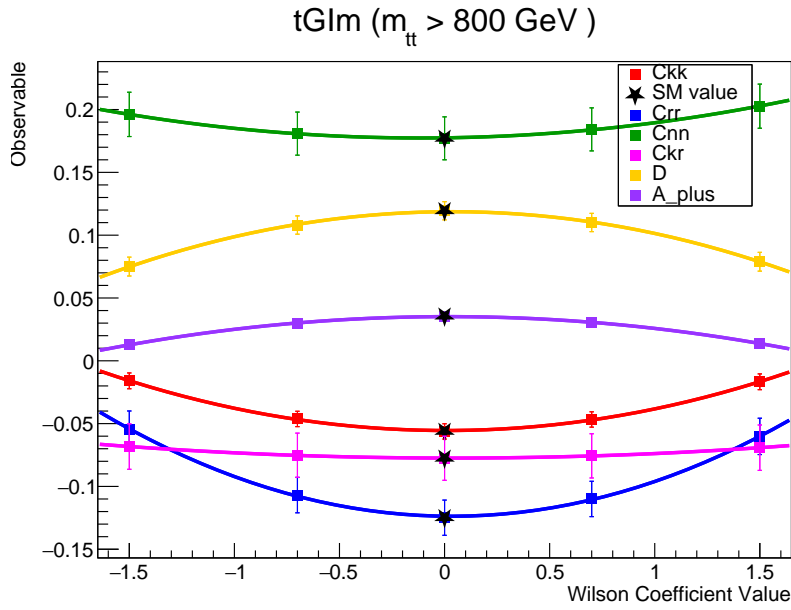
Figure 3.10: One-operator scan for tG_{Im} in the boosted region ($m_{t\bar{t}} > 800$ GeV). The SM reference point is indicated.

4 Results

The methodology described in the previous chapter is now applied to extract quantitative results for spin correlations and quantum observables in top–antitop production. The impact of dimension–6 SMEFT operators is investigated. Both single-operator and two-operator scenarios are explored, and the corresponding polynomial parametrizations are used to quantify deviations with respect to the SM. Finally, the results are interpreted in a global EFT framework using the `EFTfitter` tool, allowing for a statistical assessment of the constraining power of different observables. Finally, using the CMS values of the diagonal coefficients C_{ii} in central boosted and high boosted regime, these measurements were incorporated as inputs to the `EFTfitter` framework, where they were confronted with the polynomial parametrizations obtained for the SMEFT operators. This allowed to perform a Bayesian global fit, extract 90% credibility intervals for the WCs under study, and evaluate the relative constraining power of each observable, thereby providing a direct connection between experimental spin–correlation results and quantitative bounds on dimension–six operators.

4.1 Results of the Sensitivity Analysis

The comparison in Section 3.5.1 shows good agreement between the diagonal spin-correlation coefficients C_{ii} obtained with the methods developed in this work and the values reported by the CMS Collaboration [39]. This validation provides the basis to extend the analysis towards sensitivity studies of dimension–6 SMEFT operators, focusing on C_{kk}, C_{rr}, C_{nn}, C_{kr}, and D_3 in the threshold, boosted, central boosted, and central high-boosted regions.

In the case of the sensitivity of operators, Figs. 4.3 and 4.4 show the ratio of SMEFT to SM predictions for all the operators considered, evaluated for a specific observable in the threshold and central boosted regions, respectively. The quadratic fits to the sampled points are also displayed in the same figures.

For each identified sensitive operator, the corresponding observables were plotted as a function of the WCs. The results for the most sensitive operators are shown in Fig. 4.1 for the threshold region and in Fig. 4.2 for the boosted region. The impact of each operator on the spin-correlation observables and asymmetries can be directly assessed. Each set of figures illustrates the ratio of EFT predictions over the SM baseline as a function of the corresponding WCs. The results confirm that the impact of EFT operators strongly depends on both the energy regime and the angular cuts applied.

(a) Qj18

(b) tGIm

(c) tGRe

(d) tj8

(e) tu8
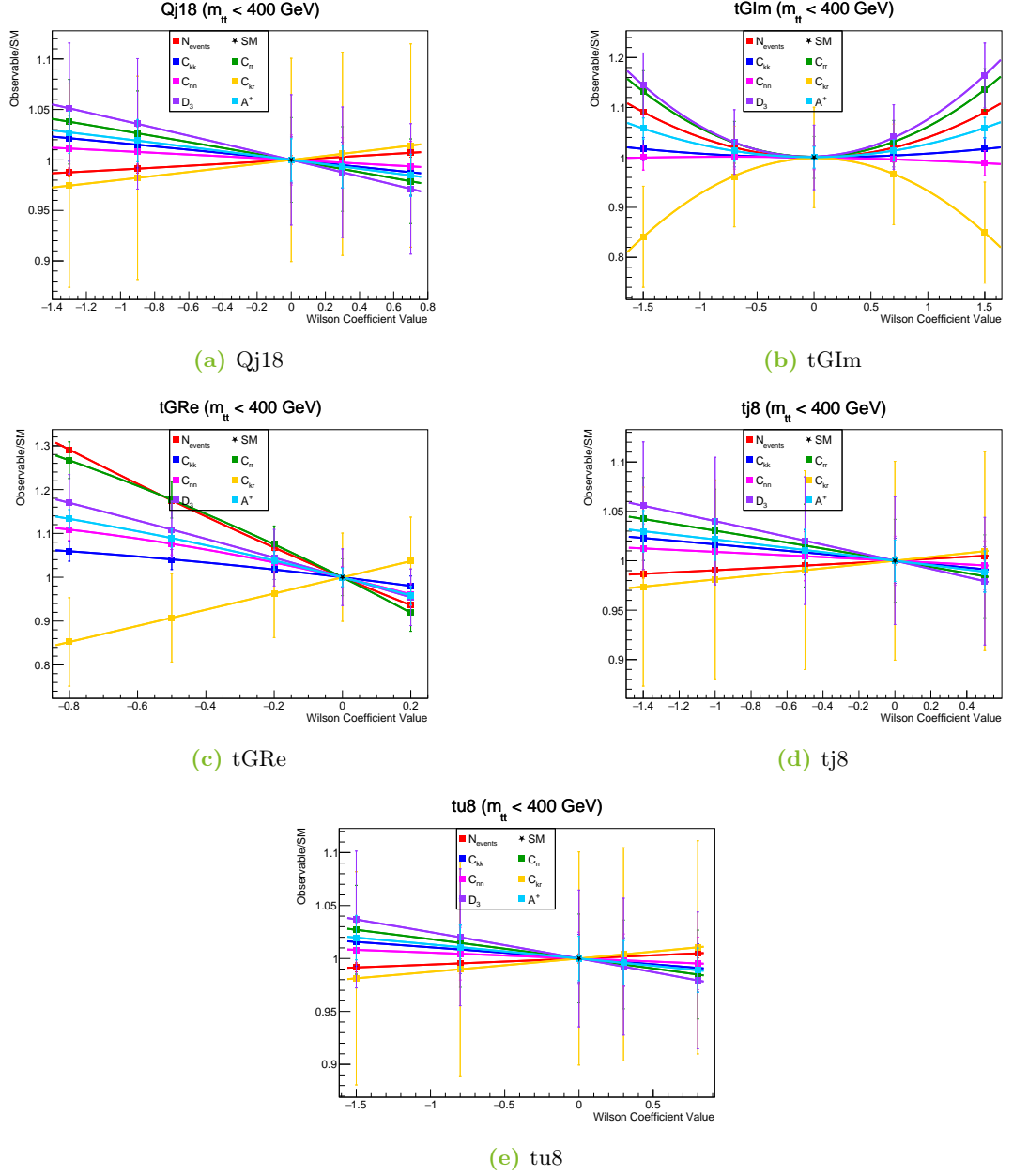
Figure 4.1: EFT effects in the threshold region ($m_{t\bar{t}} < 400\,\text{GeV}$) for different observables.

(a) Qj11

(b) Qj31

(c) Qu1

(d) tGIm

(e) tGRe
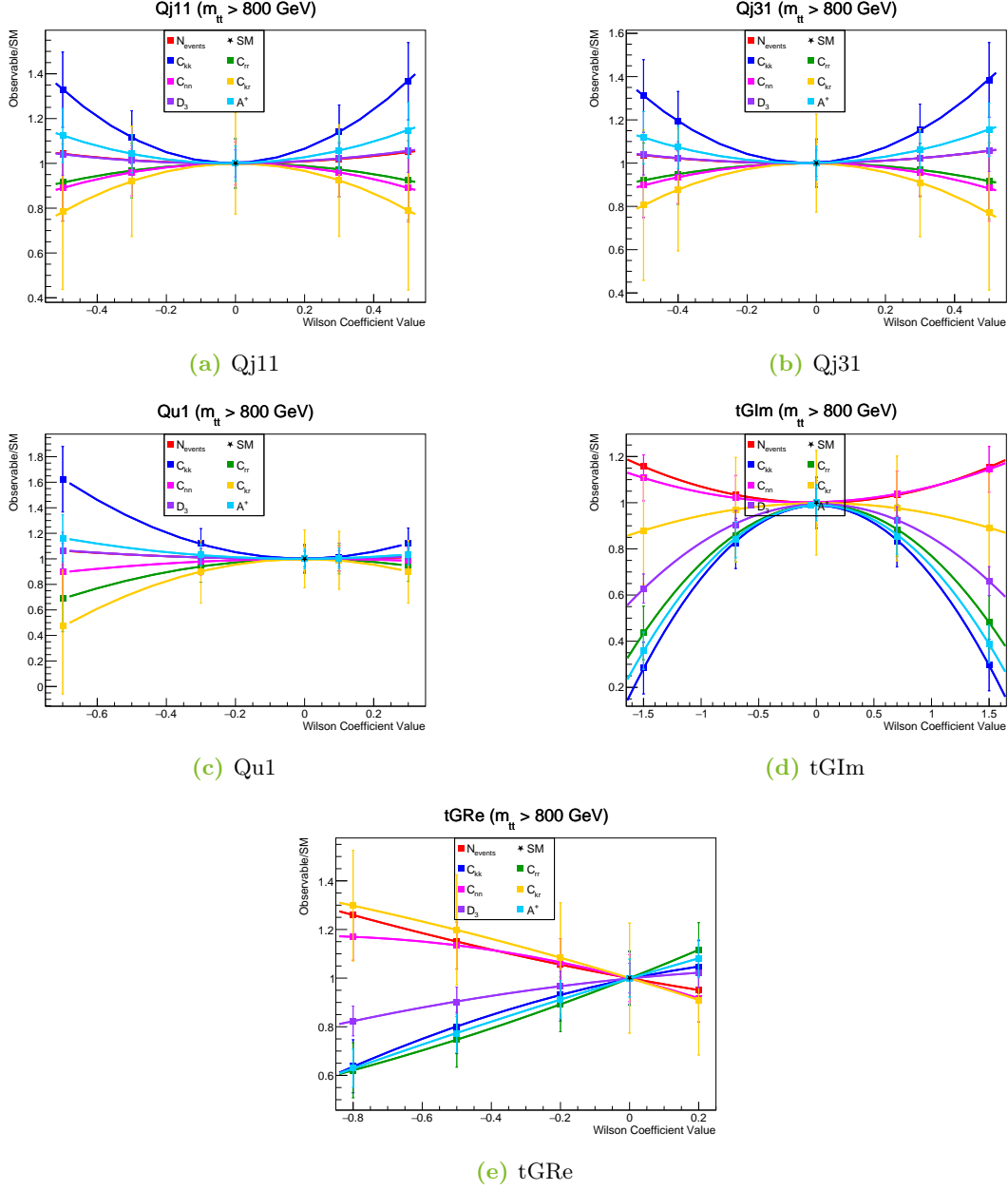
Figure 4.2: EFT effects in the boosted region ($m_{t\bar{t}} > 800\,\text{GeV}$) for different observables.

More specifically, in the threshold region (Fig. 4.3), the deviations relative to the SM are typically in the range of 10–20%. The only operator exhibiting a clear quadratic dependence on its WCs, both real and imaginary parts, is the chromomagnetic dipole operator $\mathcal{O}_{tG}$, with a leading contribution proportional to $(c_{tG}/\Lambda^2)^2$. This behavior enhances the sensitivity to deviations from the SM in this kinematic regime. By contrast, the four-fermion operators show predominantly linear dependence proportional to c/Λ^2, corresponding to SM-dimension-6 interference, without producing significant deviations from the SM expectation. The most sensitive observables in this regime are C_{kr}, D_3, and C_{rr}, along with N_{events}, and can still be used to constrain EFT effects, although the overall sensitivity remains low.

In the boosted region, the leading contribution changes substantially, with quadratic terms proportional to $(c/\Lambda^2)^2$ becoming dominant. In this regime, the four-fermion operators gain sensitivity, particularly the color-singlet operators $\mathcal{O}_{Qu}^{(1)}$, $\mathcal{O}_{Qj}^{(1,1)}$ and $\mathcal{O}_{Qj}^{(3,1)}$ with the largest distortions driven by C_{kk}. The chromomagnetic dipole operator nevertheless remains highly sensitive, with especially strong effects in N_{events}, D_3, and A^+. In general, the observables C_{kk}, C_{rr}, C_{nn}, and C_{kr} exhibit deviations as large as $40 - 60\%$, while the azimuthal asymmetry A^+ provides additional discriminatory power.

When restricting to the central boosted region Fig. 4.4, the deviations become more pronounced, reaching values of ratios SMEFT-to-SM between 0 and 2. The central angular selection suppresses forward scattering and amplifies the relative sensitivity of C_{kk} and C_{kr}, while N_{events} and A^+ also acquire strong discriminating power. This confirms the importance of angular cuts to enhance EFT reach in boosted top-pair production. The most sensitive operators remain the same as in the boosted case.

Finally, in the central highly-boosted region, the effects of EFT operators are dramatically amplified, and the dominant contribution shifts towards the four-fermion operators, with some observables showing deviations of up to a factor of 15 times with respect to the SM. In this regime, C_{kk}, C_{rr}, and C_{kr}, along with N_{events}, dominate the sensitivity. This region therefore provides the most powerful probe of SMEFT effects, although limited by reduced statistics.

Table 4.1: Results on most sensitive operators and observables per kinematic region.

| Region	Sensitive Operators	Sensitive Observables
$m_{t\bar{t}} < 400$ GeV	tG, tj8, Qj18 ,tu8,	C_{kr}, D_3, C_{rr}, N_{events}
$m_{t\bar{t}} > 800$ GeV	tG, Qu1, Qj31 ,Qj11,	C_{rr}, C_{kk}, C_{kr}, C_{nn}, A^+
$m_{t\bar{t}} > 800$ GeV, $\lvert\cos\theta\rvert < 0.4$	tG, Qj31, Qu1 ,Qj11,	C_{kr}, C_{kk}, N_{events}, A^+
$m_{t\bar{t}} > 1500$ GeV, $\lvert\cos\theta\rvert < 0.2$	Qj31, Qu1, Qj11, td1, Qj18	C_{kr}, C_{kk}, N_{events}, C_{rr}

Overall, the comparison across regions shows that no single observable or phase space dominates the sensitivity. Instead, the combination spin correlations and observables across multiple kinematic regimes is essential to fully exploit the potential of top-pair
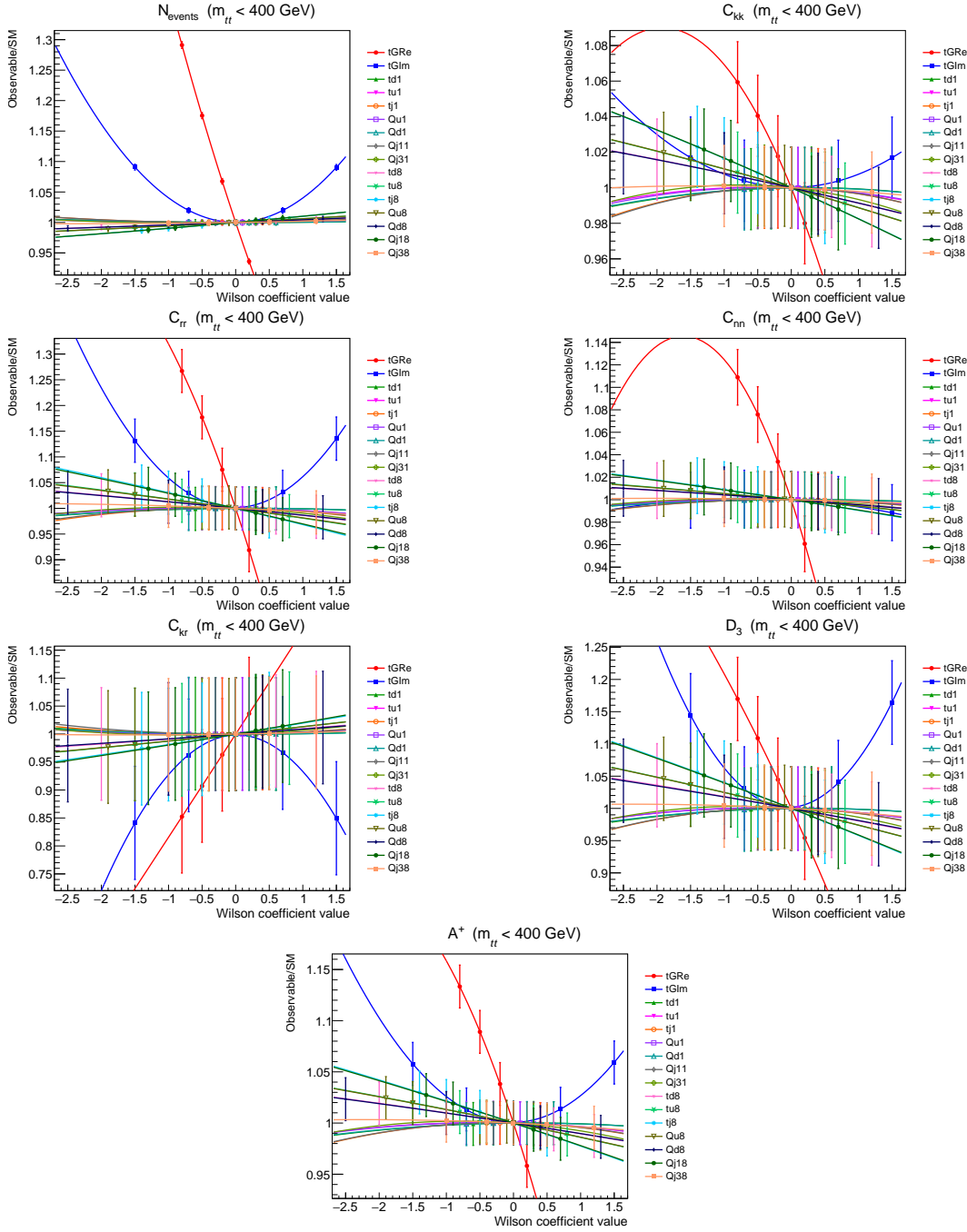
Figure 4.3: Dependence of O_{EFT}/O_{SM} on the Wilson coefficients in the threshold regime, $m_{t\bar{t}} < 400$ GeV. The observables are normalized to the SM prediction and fitted with quadratic polynomials.
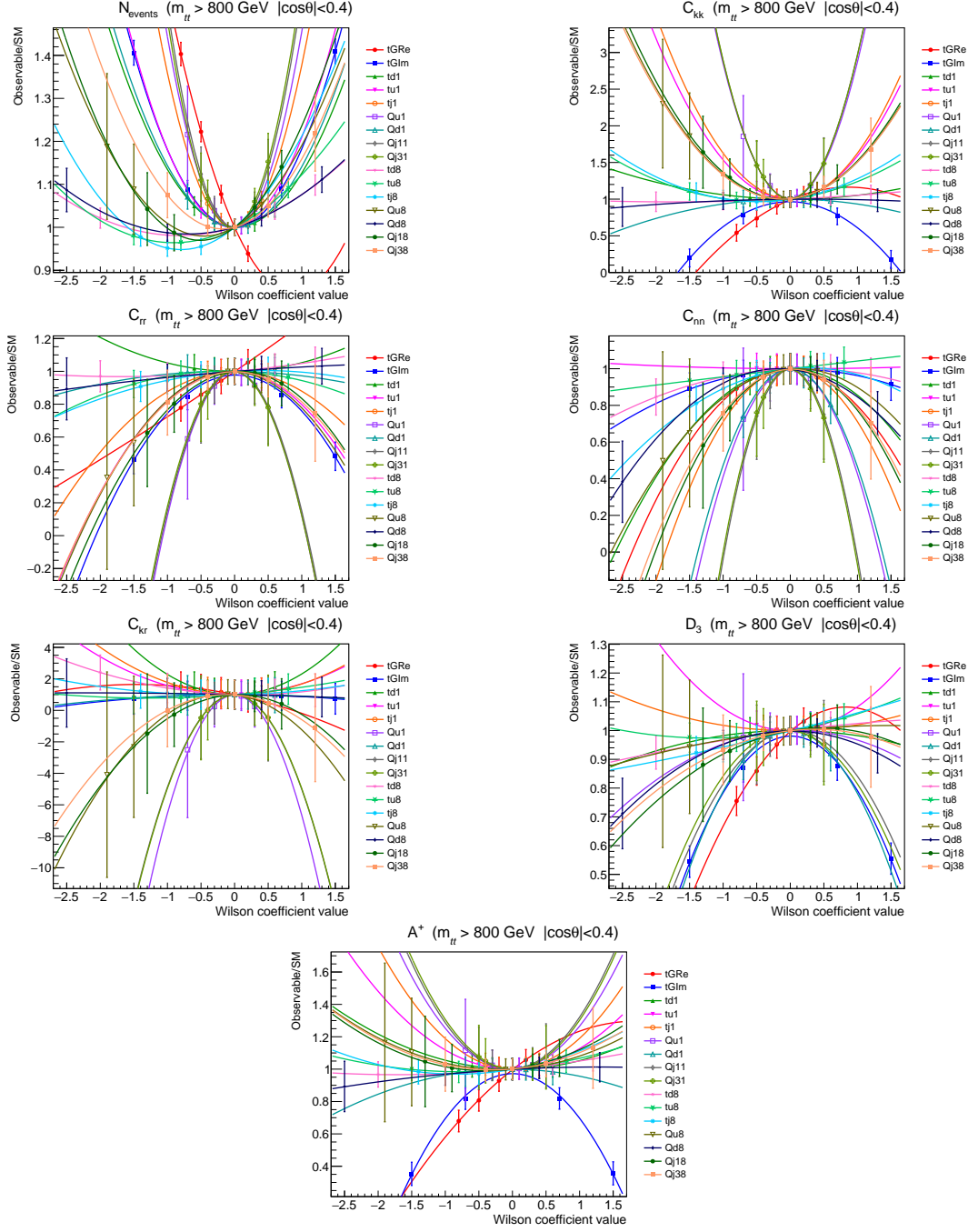
Figure 4.4: Dependence of O_{EFT}/O_{SM} on the Wilson coefficients in the central boosted regime, $m_{t\bar{t}} > 800$ GeV and $|\cos\theta| < 0.4$. The observables are normalized to the SM prediction and fitted with quadratic polynomials.

production as a laboratory for EFT effects. The overall sensitivity results are compiled in Table 4.1.

## 4.2 Constraining Power of $N_{\mathbf{events}}$ and Spin–Correlation Observables

To assess the constraining power of different observables, a dedicated comparison was performed between N_{events} and the spin correlations and quantum observables introduced in this work. The procedure was carried out with the `EFTfitter` tool. As described in Sec. 3.4.1, the implementation was done with a uniform prior probability over the available WC ranges (Fig. 3.3), a relative uncertainty of 10% was assigned to the measurements, the theoretical predictions were assumed to be error-free, and statistical uncertainties were added to the individual measurement values. No correlations between different observables were assumed.

The results consist of posterior distributions for each WC, the corresponding credible intervals, and the ranking of observables for each pair of WCs. These were obtained in three scenarios: (a) including all observables, (b) excluding N_{events}, and (c) using only N_{events} as input; and were analyzed separately in the boosted, the central boosted, and the central high-boosted regions. In the ranking method, each observable is removed from the fit one at a time and the analysis is repeated. The ranking value is then defined as the relative increase of the 90% posterior credible interval width for the WCs, compared to the full fit including all observables.

Results show that in the central high-boosted regime, the posterior distributions are dominated by the observable N_{events}, ranking as the most constraining observable, meanwhile in the boosted and central boosted regime the observables that provide the dominant sensitivity are the diagonal C_{ii}. The ranking comparison of boosted and central high-boosted regions for the pair (C_{Qj38}, C_{Qj31}) and (C_{td8}, C_{Qd8}) shown in Figs. 4.5 and 4.6 illustrates this result. A larger bar indicates that the corresponding observable plays a more important role in constraining the EFT parameter space: in the boosted region, C_{kk} and C_{nn} dominate for each pair, while in the central high-boosted region N_{events} is the leading constraint for both pairs.

In general, C_{kk} provides the most stringent bounds in the boosted region, which leads to nearly circular or horizontally aligned elliptical contours for coefficients such as C_{Qj38} (Fig. 4.7), as well as for C_{Qu8} and C_{td8}. This indicates that these observables constrain the corresponding WCs almost independently, with minimal degeneracy. When C_{nn} drives the sensitivity, the posteriors become flattened or tilted, reflecting stronger correlations and degeneracies between operators. Fits where C_{rr} contributes most strongly display more asymmetric or skewed contours, indicating that the constraints are anisotropic.

(a) Boosted region

(b) Central high-boosted region
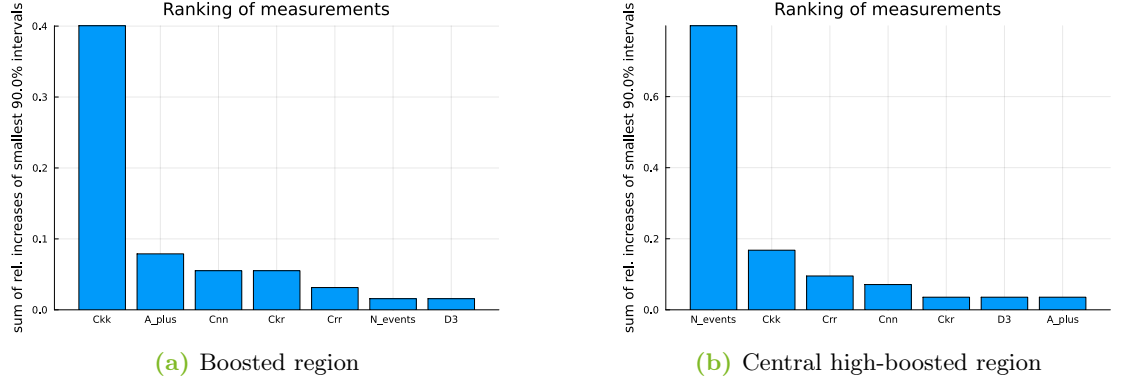
Figure 4.5: Comparison of ranking results for operators `Qj38` and `Qj31` in two kinematic regions. Each histogram shows the relative impact of observables on the posterior width.

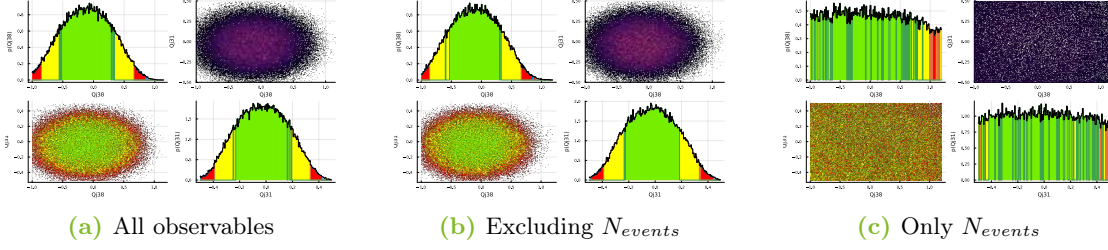**(a)** Boosted region

(b) Central high-boosted region
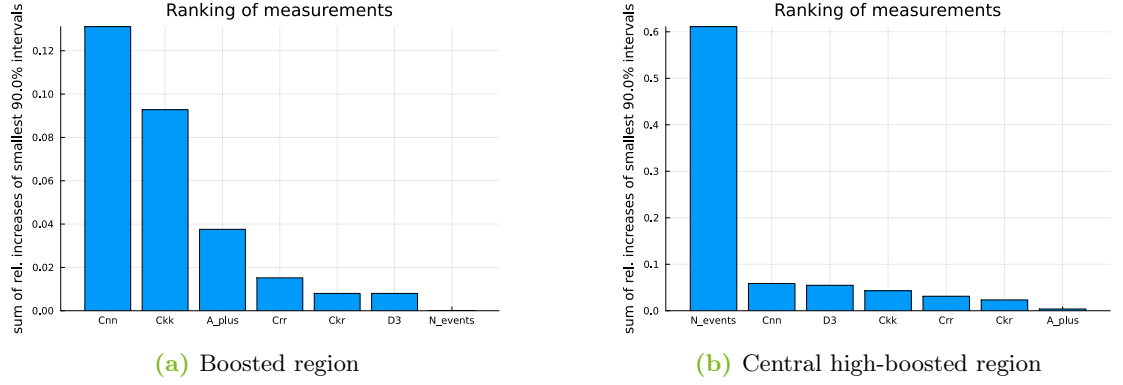
Figure 4.6: Comparison of ranking results for operators `td8` and `Qd8` in two kinematic regions. Each histogram shows the relative impact of observables on the posterior width.

The observable N_{events} alone yields flat posteriors in the boosted regime, as shown in Fig. 4.7c for the (C_{Qj38}, C_{Qj31}) pair, demonstrating its negligible constraining power. Furthermore, when added to the global fit including spin observables, the posteriors show no appreciable change, as shown in Fig. 4.7b for the same pair.
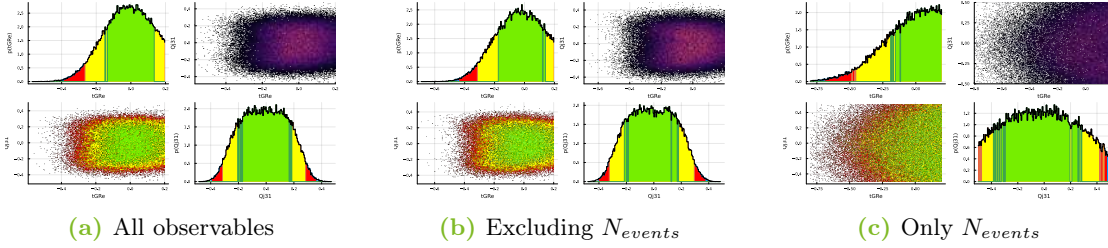
The results in the central boosted region show the same qualitative behavior as in the boosted region, with C_{kk} and C_{nn} providing the dominant sensitivity. When C_{nn} dominates, the posteriors exhibit strong correlations and degeneracies, so the coefficients cannot be constrained independently. In contrast, when C_{kk} dominates, both coefficients show low correlation. Finally, N_{events} becomes more relevant in planes involving C_{tGRe}, where its combination with spin observables distorts the posterior shapes, as shown in Fig. 4.8.

(a) All observables   **(b)** Excluding N_{events} **(c)** Only N_{events}
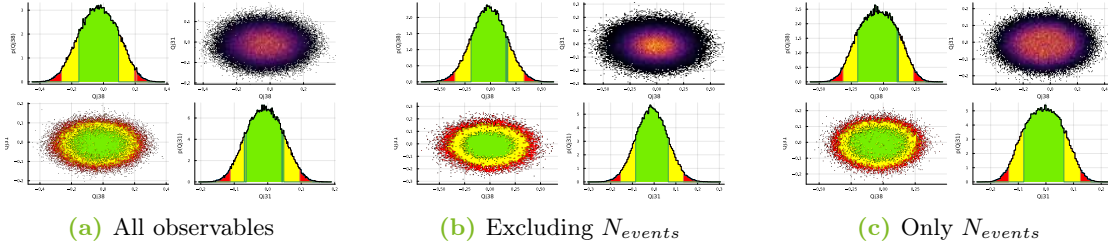
Figure 4.7: Posterior distributions for C_{Qj38} and C_{Qj31} in the boosted region. Results are shown including all observables, excluding N_{events}, or using only N_{events}.

(a) All observables   **(b)** Excluding N_{events} **(c)** Only N_{events}
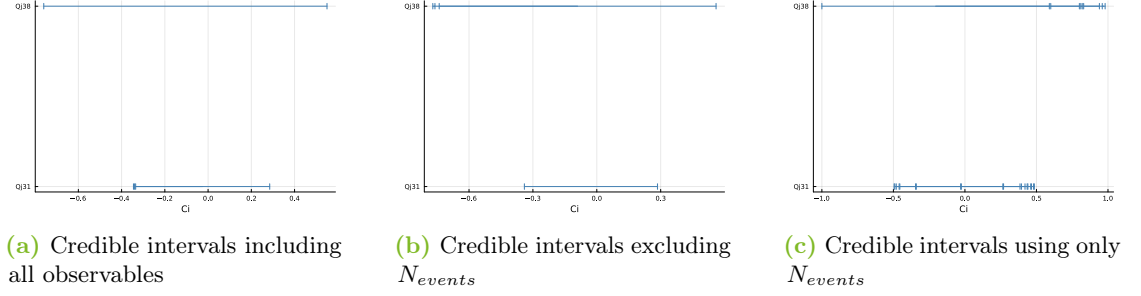
Figure 4.8: Posterior distributions for C_{tGRe} and C_{Qj31} in the central boosted region. Results are shown including all observables, excluding N_{events}, or using only N_{events}.

In the central high-boosted regime the two-dimensional posteriors frequently display complex non-elliptical structures when all observables are included, such as split peaks or deformed contours. Among the operator pairs, (C_{Qj38}, C_{Qj31}) shown in Fig. 4.9, as well as (C_{Qj38}, C_{Qu8}) and (C_{Qj18}, C_{Qu8}), exhibit an elliptical shape with a mild horizontal elongation, indicating weaker correlations and consistent parameter constraints, which become further sharpened when N_{events} is included.

(a) All observables   **(b)** Excluding N_{events} **(c)** Only N_{events}

Figure 4.9: Posterior distributions for C_{Qj38} and C_{Qj31} in the central high-boosted region. Results are shown including all observables, excluding N_{events}, or using only N_{events}.

(a) Credible intervals including all observables

(b) Credible intervals excluding N_{events}

(c) Credible intervals using only N_{events}

Figure 4.10: Smallest 90% credible intervals for C_{Qj38} and C_{Qj31} in the boosted region. The impact of N_{events} is explicitly shown.

(a) Credible intervals including all observables

(b) Credible intervals excluding N_{events}

(c) Credible intervals using only N_{events}
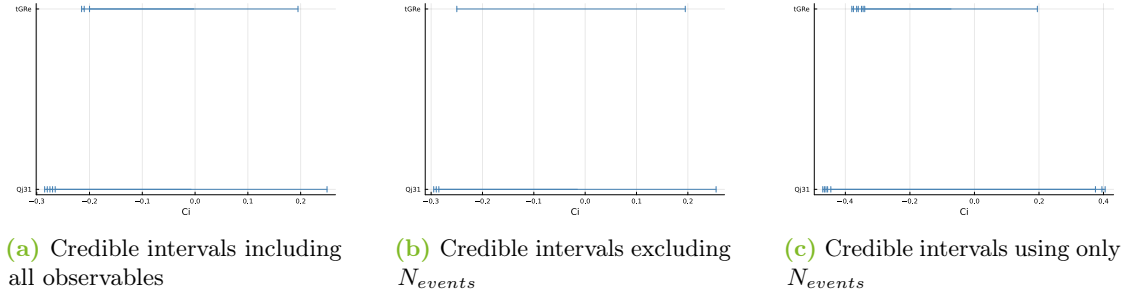
Figure 4.11: Smallest 90% credible intervals for C_{tGRe} and C_{Qj31} in the central boosted region. The impact of N_{events} is explicitly shown.

(a) Credible intervals including all observables

(b) Credible intervals excluding N_{events}

(c) Credible intervals using only N_{events}
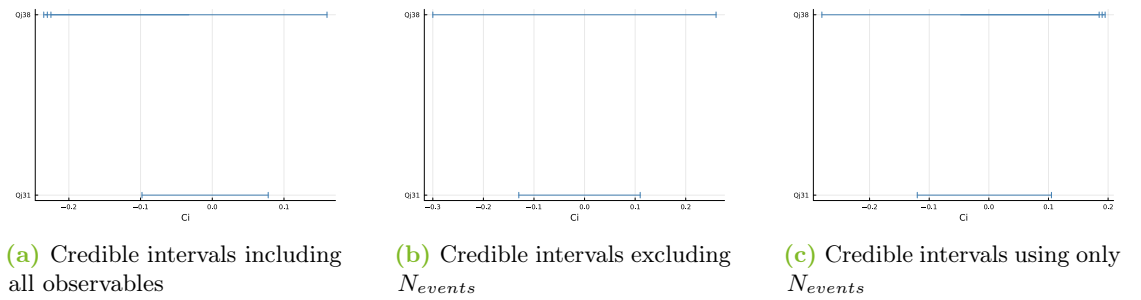
Figure 4.12: Smallest 90% credible intervals for C_{Qj38} and C_{Qj31} in the central high-boosted region. The impact of N_{events} is explicitly shown.

In summary, the comparison of N_{events} with spin–correlation observables shows that the latter provide the dominant sensitivity across most kinematic regimes, with C_{kk} leading to nearly independent constraints and C_{nn} driving stronger correlations and degeneracies. C_{rr} contributes less effectively, producing more anisotropic posteriors. In the boosted and central boosted regions, N_{events} alone has negligible constraining power and does not significantly alter the global fits. However, in the central high-boosted regime N_{events} gains importance, sharpening the posterior contours and helping to define clearer structures for some operator pairs. Finally, the results obtained for the 90% confidence intervals, Figs. 4.10-4.12, reflects this behavior.

These results confirm that spin observables are the main drivers of sensitivity, while N_{events} plays a secondary but non-negligible role in certain regions of phase space.

4.3 Results With CMS Data

To derive quantitative constraints on the WCs, the CMS measurements of the spin-correlation coefficients C_{kk}, C_{rr}, and C_{nn} at high invariant mass ($m_{t\bar{t}} > 800$ GeV), both with and without the angular cut $|\cos\theta| < 0.4$, were used as input to the `EFTfitter` framework. Bayesian fits of pairs of WCs were then performed using the EFT parameterizations described in Section 3.4.1, with flat priors imposed within the ranges covered by the SMEFT samples.

To properly account for the correlations among the observables, the full covariance matrices reported by CMS [39], including both statistical and systematic uncertainties, were implemented, as shown in Eqs. 4.1 and 4.2.

$$\text{Cov}_{|\cos\theta|<0.4} = \begin{pmatrix} 0.01376 & -0.00036 & 0.00014 \\ -0.00036 & 0.00694 & 0.00005 \\ 0.00014 & 0.00005 & 0.00415 \end{pmatrix} \tag{4.1}$$

$$\text{Cov}_{\text{no cut}} = \begin{pmatrix} 0.00189 & -0.00006 & 0.00005 \\ -0.00006 & 0.00080 & -0.00004 \\ 0.00005 & -0.00004 & 0.00252 \end{pmatrix} \tag{4.2}$$

For each operator pair presented in Section 3.3.2, three complementary outputs are obtained: posterior distributions, credible intervals at 90% credibility levels, and rankings of the experimental observables.

Representative EFTfitter results based on CMS inputs are shown in Figs. 4.13–4.18. Each figure corresponds to a specific pair of operators and presents: (a) one-dimensional posteriors and (b) credible intervals at 90% credibility levels. All results correspond to the boosted region.

The posteriors extracted from CMS data are consistent with the SM expectation, i.e. centered at 0, and constitute EFT limits derived from spin-correlation data. Among

(a) Posterior   (b) Intervals
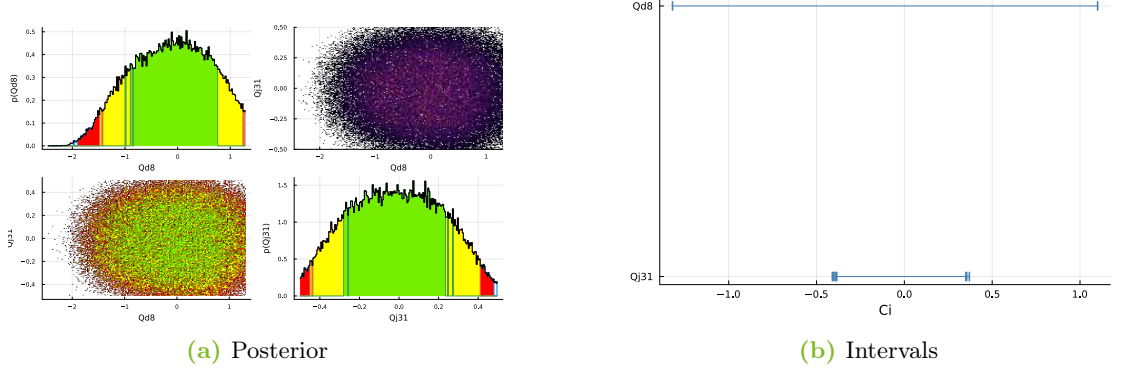
Figure 4.13: EFTfitter results for C_{Qd8}, C_{Qj31} in the boosted region.


(a) Posterior   (b) Intervals
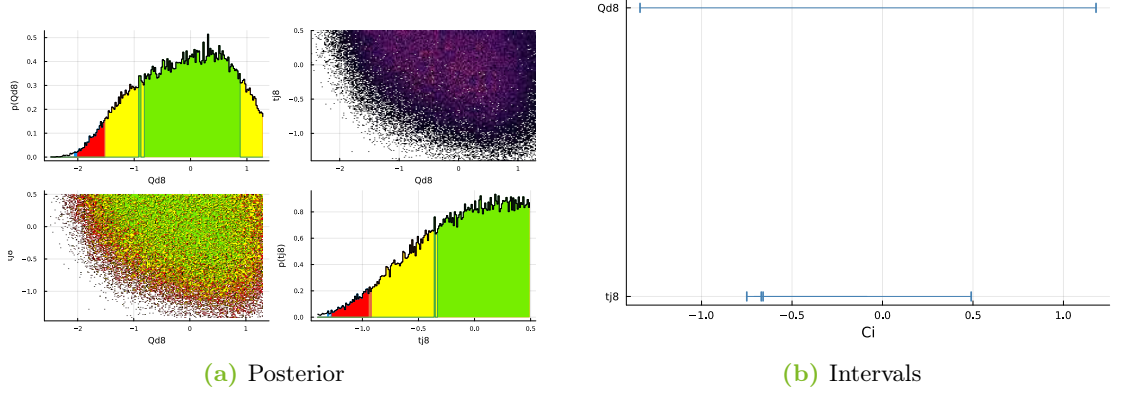
Figure 4.14: EFTfitter results for C_{Qd8}, C_{tj8} in the boosted region.

the two investigated kinematic regimes, the central boosted region emerges as the most sensitive.

In this region, C_{rr} emerges as the most constraining observable for a wide range of operator combinations, particularly when $\mathcal{O}_{Qj}^{(1,8)}$, $\mathcal{O}_{Qj}^{(3,1)}$, or $\mathcal{O}_{Qj}^{(3,8)}$ appear together with $\mathcal{O}_{Qu}^{(8)}$, $\mathcal{O}_{tj}^{(8)}$, or $\mathcal{O}_{tG}$. For other operator pairs, C_{nn} provides the leading sensitivity, while N_{events} and A^{+} gain relevance in highly boosted scenarios.

he central result of the CMS-based analysis is summarized in Table 4.2, which reports the 90% credibility intervals obtained for each WCs analyzed, and constitute the main quantitative outcome of the CMS-based analysis. A graphical representation is provided in Fig. 4.19, where the interval width directly reflects the strength of the constraint: narrower intervals correspond to stronger bounds.

Figure 4.19 and Table 4.2 show that C_{tGRe} and C_{Qj31} yield the strongest individual constraints, with allowed ranges of about ± 0.3 around zero. This indicates that the

(a) Posterior   (b) Intervals
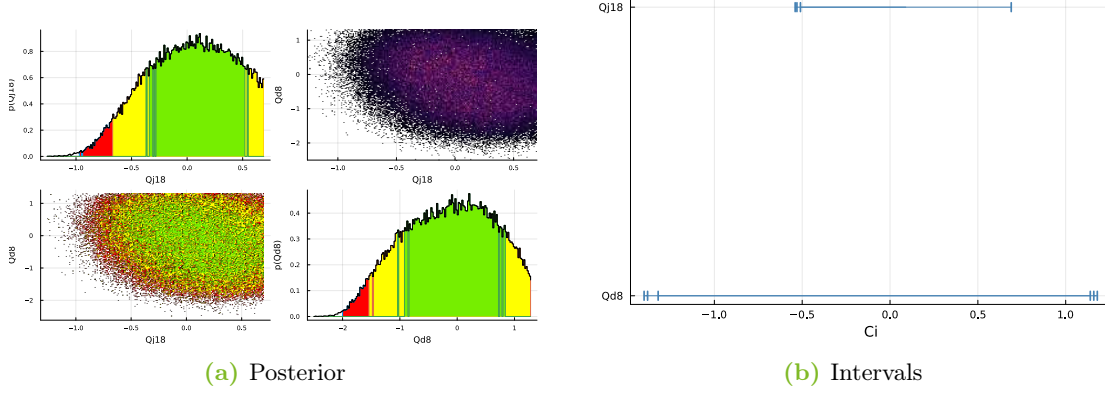
Figure 4.15: EFTfitter results for C_{Qj18}, C_{Qd8} in the boosted region.


(a) Posterior   (b) Intervals
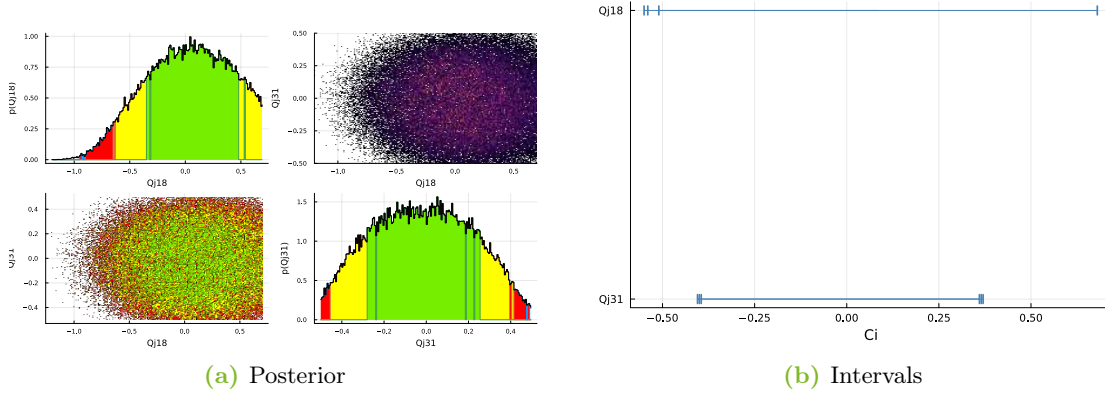
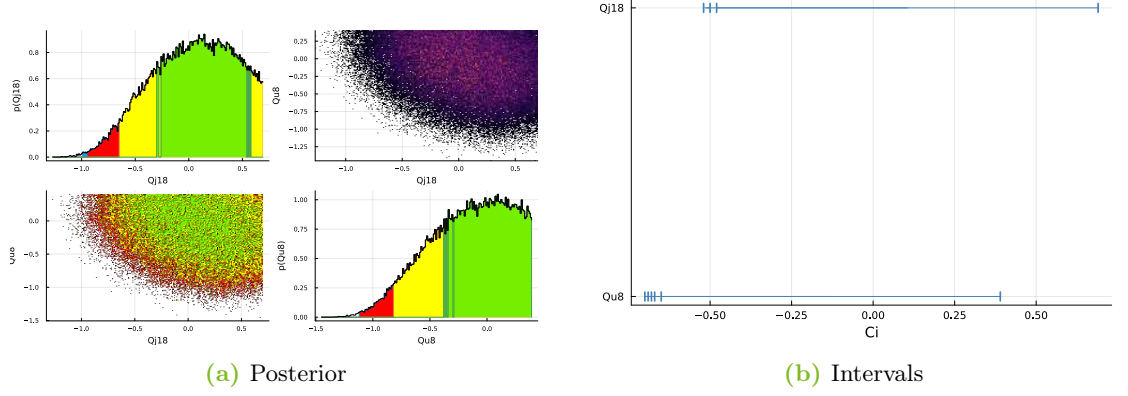**Figure 4.16:** EFTfitter results for C_{Qj18}, C_{Qj31} in the boosted region.

data confine them to values very close to the SM expectation. Intermediate sensitivity is obtained for C_{Qj18}, C_{Qu8}, and C_{Qj38}, whose intervals remain at the level of ~ 0.5–1.0. In contrast, the weakest bounds are observed for C_{Qd8}, C_{td8}, C_{tj8}, and especially C_{tu8}, which retains an allowed region broader than ~ 2, leaving it only loosely constrained by the present data.

In general, the inclusion of the angular cut $|\cos\theta| < 0.4$ improves the bounds, most visibly for C_{Qj31} and C_{Qu8}, where the allowed ranges shrink by $\sim 30\%$ compared to the boosted regime. This illustrates how selecting specific kinematic regions can increase the sensitivity of spin–correlation measurements to new physics for this specific operators.

(a) Posterior
(b) Intervals
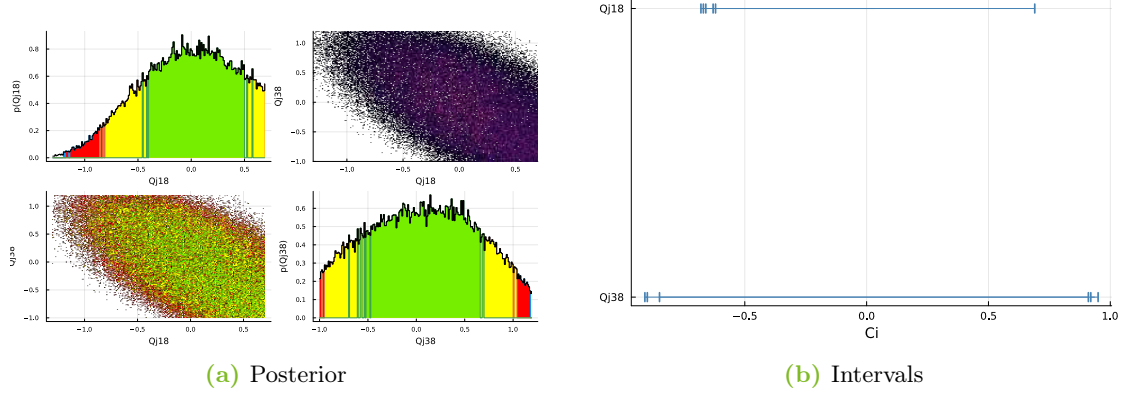
Figure 4.17: EFTfitter results for C_{Qj18}, C_{Qj38} in the boosted region.

(a) Posterior
(b) Intervals

Figure 4.18: EFTfitter results for C_{Qj18}, C_{Qu8} in the boosted region.

Parameter	Range with angle cut	Range with no angle cut
C_{Qd8}	$[-1.08, 0.78]$	$[-1.36, 1.20]$
C_{Qj18}	$[-0.49, 0.51]$	$[-0.54, 0.69]$
C_{Qj31}	$[-0.24, 0.22]$	$[-0.41, 0.36]$
C_{Qj38}	$[-0.54, 0.50]$	$[-0.84, 0.86]$
C_{Qu8}	$[-0.54, 0.39]$	$[-0.84, 0.39]$
C_{tGRe}	$[-0.24, 0.20]$	$[-0.24, 0.19]$
C_{td8}	$[-1.36, 1.18]$	$[-1.30, 1.18]$
C_{tj8}	$[-0.82, 0.49]$	$[-0.78, 0.49]$
C_{tu8}	$[-1.24, 0.64]$	$[-1.24, 0.78]$

Table 4.2: Results of best 90% credible intervals (narrowest) for Wilson coefficients. The results are compared with and without $|\cos\theta| < 0.4$ cut at $m_{t\bar{t}} > 800$ GeV.
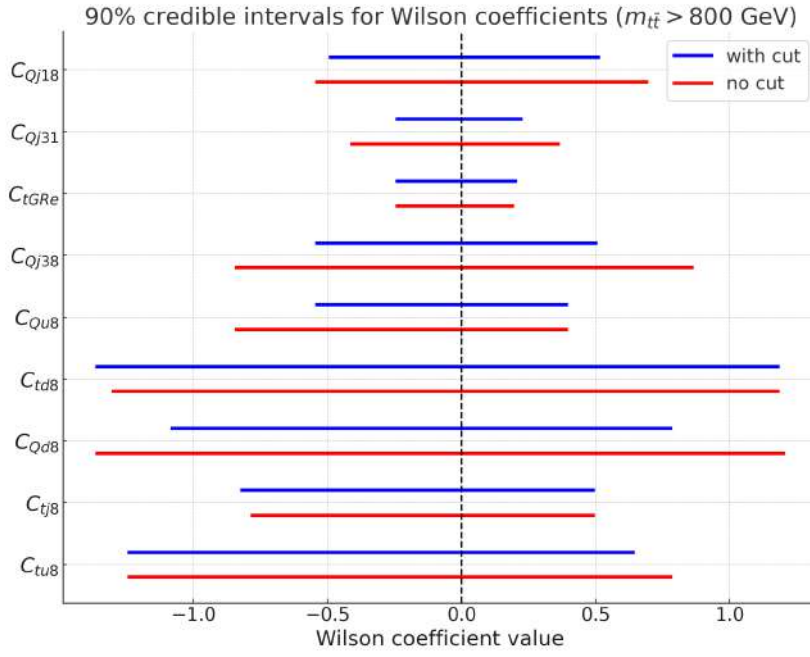
Figure 4.19: Results of 90% credible intervals for WCs obtained. Results are shown with (blue) and without (red) the angular cut $|\cos\theta| < 0.4$ in the boosted region.

5 Conclusion

This work explored the potential of quantum observables as tools to search for new physics in boosted top–quark pair production. Using next-to-leading-order QCD simulations, the spin–correlation coefficients C_{ij} were reconstructed and derived observables such as D_3 and the azimuthal asymmetry A^+ were extracted, with their behavior analyzed across distinct kinematic regions.

The results show that the central boosted regime is the most sensitive for the observation of quantum entanglement in the $t\bar{t}$ system, with the observable D_3 exceeding the critical value $1/3$. The diagonal correlations C_{ii} also become significantly more sensitive at higher energies and under angular cuts.

The introduction of dimension–six operators within the SMEFT framework enabled the quantification of deviations from the SM. Both individual and combined operator effects were studied, identifying cases that produce appreciable modifications in spin and entanglement observables, particularly in the boosted regime. The subsequent application of `EFTfitter` translated these effects into bounds on the WCs, showing that specific kinematic selections such as $|\cos\theta| < 0.4$ significantly improve sensitivity, reducing the allowed intervals for certain operators by up to 30%.

Based on the CMS measurements of spin–correlations at high invariant mass, experimental bounds on WCs were derived. The boosted, and in particular the central boosted regime emerges as the most constraining, with C_{rr} and C_{nn} identified as the leading observables in this region. The inclusion of the angular cut $|\cos\theta| < 0.4$ further tightens the allowed ranges for several operators, while certain couplings remain only weakly bounded. The comparison with CMS data demonstrates that spin–correlation measurements already provide illustrative EFT limits and highlight the potential of quantum observables to become a central element in future global analyses of the top sector.

While the results are encouraging, several limitations must be acknowledged. The available statistics in the highly boosted regime remain limited, preventing robust statements about entanglement and Bell-inequality violation in this region. Finally, the interpretation relies on the SMEFT truncated at dimension–six operators, which may not fully capture higher-order effects.

Future developments should therefore include detector-level simulations, the use of the full ATLAS and CMS datasets, and the exploration of complementary observables. .

In this light, the present study highlights both the feasibility and the scientific impact of bringing quantum-inspired tools into collider physics. Quantum observables in top–quark pair production emerge as a complementary and powerful probe to traditional analyses based on total and differential cross sections. Within the EFT framework, they already

provide meaningful bounds on WCs from LHC data and emphasize their potential role in future global SMEFT analyses of the top sector.

Bibliography

[1] C. Severi and E. Vryonidou. "Quantum entanglement and top spin correlations in SMEFT at higher orders". In: *JHEP* 2023.1 (2023), p. 148. DOI: 10.1007/JHEP01(2023)148.

[2] ATLAS Collaboration and CMS Collaboration. "Combination of Measurements of the Top Quark Mass from Data Collected by the ATLAS and CMS Experiments at $\sqrt{s} = 7$ and 8 TeV". In: *Phys. Rev. Lett.* 132.26 (2024), p. 261902. DOI: 10.1103/PhysRevLett.132.261902.

[3] ATLAS Collaboration. "Observation of Spin Correlation in $t\bar{t}$ Events from pp Collisions at $\sqrt{s} = 7$ TeV Using the ATLAS Detector". In: *Phys. Rev. Lett.* 108 (2012), p. 212001. DOI: 10.1103/PhysRevLett.108.212001.

[4] ATLAS Collaboration. "Measurements of spin correlation in top-antitop quark events from proton-proton collisions at $\sqrt{s} = 7$ TeV using the ATLAS detector". In: *Phys. Rev. D* 90 (2014), p. 112016. DOI: 10.1103/PhysRevD.90.112016.

[5] CMS Collaboration. "Measurement of spin correlations in $t\bar{t}$ production using the matrix element method in the muon+jets final state in pp collisions at $\sqrt{s} = 8$ TeV". In: *Phys. Lett. B* 758 (2016), pp. 321–346. DOI: 10.1016/j.physletb.2016.05.005.

[6] CMS Collaboration. "Measurements of $t\bar{t}$ spin correlations and top quark polarization using dilepton final states in pp collisions at $\sqrt{s} = 8$ TeV". In: *Phys. Rev. D* 93 (2016), p. 052007. DOI: 10.1103/PhysRevD.93.052007.

[7] ATLAS Collaboration. "Probing the spin correlations of top quark pairs at $\sqrt{s} = 13$ TeV with the ATLAS detector". In: *JHEP* 03 (2017), p. 113. DOI: 10.1007/JHEP03(2017)113.

[8] CMS Collaboration. "Measurement of the top quark polarization and $t\bar{t}$ spin correlations using dilepton final states in proton-proton collisions at $\sqrt{s} = 13$ TeV". In: *Phys. Rev. D* 100 (2019), p. 072002. DOI: 10.1103/PhysRevD.100.072002.

[9] ATLAS Collaboration. "Measurements of top-quark pair spin correlations in the $e\mu$ channel at $\sqrt{s} = 13$ TeV using 36 fb^{-1} of ATLAS data". In: *Eur. Phys. J. C* 80 (2020), p. 754. DOI: 10.1140/epjc/s10052-020-7907-9.

[10] ATLAS Collaboration. "Measurements of top-quark pair spin observables at $\sqrt{s} = 13$ TeV with the ATLAS detector". In: *Eur. Phys. J. C* 80 (2020), p. 681. DOI: 10.1140/epjc/s10052-020-8181-6.

[11] F. Quevedo and A. Schachner. *Cambridge Lectures on The Standard Model*. 2024. arXiv: 2409.09211 [hep-th].

[12] I. Neutelings. *Standard Model decay pie chart*. Licensed under CC BY-SA 4.0. 2021. URL: https://tikz.net/sm_decay_piechart/.

[13] C. Burgess and G. Moore. *The Standard Model: A Primer*. Cambridge University Press, 2007.

[14] R. Aaij et al. "Observation of $J/\psi p$ Resonances Consistent with Pentaquark States in $\Lambda_b^0 \to J/\psi K^- p$ Decays". In: *Phys. Rev. Lett.* 115.7 (2015), p. 072001. DOI: 10.1103/PhysRevLett.115.072001. arXiv: 1507.03414 [hep-ex].

[15] R. Aaij et al. "Observation of structure in the J/ψ-pair mass spectrum". In: *Sci. Bull.* 65 (2020), pp. 1983–1993. DOI: 10.1016/j.scib.2020.08.032. arXiv: 2006.16957 [hep-ex].

[16] M. Kobayashi and T. Maskawa. "CP Violation in the Renormalizable Theory of Weak Interaction". In: *Prog. Theor. Phys.* 49 (1973), pp. 652–657. DOI: 10.1143/PTP.49.652.

[17] CDF Collaboration. "Observation of Top Quark Production in $\overline{p}p$ Collisions with the Collider Detector at Fermilab". In: *Phys. Rev. Lett.* 74.14 (1995), pp. 2626–2631. DOI: 10.1103/PhysRevLett.74.2626.

[18] D0 Collaboration. "Search for High Mass Top Quark Production in $p\overline{p}$ Collisions at $\sqrt{s} = 1.8$ TeV". In: *Phys. Rev. Lett.* 74.13 (1995), pp. 2422–2426. DOI: 10.1103/PhysRevLett.74.2422.

[19] S. Navas et al. "Review of Particle Physics". In: *Phys. Rev. D* 110 (2024). 2025 update, p. 030001. DOI: 10.1103/PhysRevD.110.030001.

[20] Z. Dong et al. "When the machine chimes the Bell: entanglement and Bell inequalities with boosted $t\bar{t}$". In: *arXiv preprint* (2023). arXiv: 2305.07075 [hep-ph].

[21] P. Kaye, R. Laflamme, and M. Mosca. *An Introduction to Quantum Computing*. OUP Oxford, 2006.

[22] G. Mahlon and S. J. Parke. "Spin correlation effects in top quark pair production at the LHC". In: *Phys. Rev. D* 81.7 (2010), p. 074024. DOI: 10.1103/PhysRevD.81.074024.

[23] W. Bernreuther and Z.-G. Si. "Distributions and correlations for top quark pair production and decay at the Tevatron and LHC". In: *Nucl. Phys. B* 837.1–2 (2010), pp. 90–121. DOI: 10.1016/j.nuclphysb.2010.05.001.

[24] M. Jeżabek. "Top quark physics". In: *Nucl. Phys. B Proc. Suppl.* 37.2 (1994), pp. 197–212. DOI: 10.1016/0920-5632(94)90677-7.

[25] B. Tweedie. "Better hadronic top quark polarimetry". In: *Phys. Rev. D* 90.9 (2014), p. 094010. DOI: 10.1103/PhysRevD.90.094010.

[26] W. Bernreuther, D. Heisler, and Z.-G. Si. "A set of top quark spin correlation and polarization observables for the LHC: Standard Model predictions and new physics contributions". In: *JHEP* 2015.12 (2015), p. 026. DOI: 10.1007/JHEP12(2015)026.

[27] A. J. Barr et al. *Quantum entanglement and Bell inequality violation at colliders.* 2024. arXiv: 2402.07972 [hep-ph].

[28] CMS Collaboration. "Measurements of polarization and spin correlation and observation of entanglement in top quark pairs using ℓ+jets events from proton-proton collisions at $\sqrt{s} = 13$ TeV". In: *Phys. Rev. D* 110.11 (2024), p. 112016. DOI: 10.1103/PhysRevD.110.112016.

[29] J. A. Aguilar-Saavedra et al. *Interpreting top-quark LHC measurements in the Standard-Model Effective Field Theory.* LHC TOP WG note, CERN-LPCC-2018-01. 2018. arXiv: 1802.07237 [hep-ph].

[30] J. S. Bell. "On the Einstein Podolsky Rosen paradox". In: *Physics Physique Fizika* 1 (3 Nov. 1964), pp. 195–200. DOI: 10.1103/PhysicsPhysiqueFizika.1.195.

[31] T. Han, M. Low, and T. A. Wu. *Quantum Entanglement and Bell Inequality Violation in Semi-Leptonic Top Decays.* 2023. arXiv: 2310.17696 [hep-ph].

[32] B. Grzadkowski et al. "Dimension-six terms in the Standard Model Lagrangian". In: *JHEP* 2010.10 (2010), p. 085. DOI: 10.1007/JHEP10(2010)085.

[33] ATLAS Collaboration. *Monte Carlo Simulation.* https://atlas.cern. Accessed: 2025-09-07.

[34] J. Alwall et al. "The automated computation of tree-level and next-to-leading order differential cross sections, and their matching to parton shower simulations". In: *JHEP* 07 (2014), p. 079. DOI: 10.1007/JHEP07(2014)079. arXiv: 1405.0301 [hep-ph].

[35] T. Sjöstrand et al. "An Introduction to PYTHIA 8.2". In: *Comput. Phys. Commun.* 191 (2015), pp. 159–177. DOI: 10.1016/j.cpc.2015.01.024. arXiv: 1410.3012 [hep-ph].

[36] I. Brivio and M. Trott. "The SMEFTsim package, theory and tools". In: *JHEP* 04 (2019), p. 073. DOI: 10.1007/JHEP04(2019)073. arXiv: 1709.06492 [hep-ph].

[37] S. Alioli et al. "A general framework for implementing NLO calculations in shower Monte Carlo programs: the POWHEG BOX". In: *JHEP* 06 (2010), p. 043. DOI: 10.1007/JHEP06(2010)043. arXiv: 1002.2581 [hep-ph].

[38] J. Jamieson et al. *Differential cross-section measurements of boosted top quarks in the ℓ+jets channel in pp collisions at $\sqrt{s} = 13$ TeV using the ATLAS detector.* Tech. rep. Geneva: CERN, 2020.

[39] CMS Collaboration. "Measurements of polarization and spin correlation and observation of entanglement in top quark pairs using lepton+jets events from proton-proton collisions at $\sqrt{s}$ = 13 TeV". In: *Phys. Rev. D* 110.11 (2024), p. 112016. DOI: 10.1103/PhysRevD.110.112016. arXiv: 2409.11067 [hep-ex].

Eidesstattliche Versicherung

(Affidavit)

Elizalde Palacios, Josue Salvador

Name, Vorname
(surname, first name)

258621

Matrikelnummer
(student ID number)

☐ Bachelorarbeit
(Bachelor's thesis)

■ Masterarbeit
(Master's thesis)

Titel
(Title)

Exploring the potential of quantum observables to search for new physics, in boosted top-pair production

---

Ich versichere hiermit an Eides statt, dass ich die vorliegende Abschlussarbeit mit dem oben genannten Titel selbstständig und ohne unzulässige fremde Hilfe erbracht habe. Ich habe keine anderen als die angegebenen Quellen und Hilfsmittel benutzt sowie wörtliche und sinngemäße Zitate kenntlich gemacht. Die Arbeit hat in gleicher oder ähnlicher Form noch keiner Prüfungsbehörde vorgelegen.

I declare in lieu of oath that I have completed the present thesis with the above-mentioned title independently and without any unauthorized assistance. I have not used any other sources or aids than the ones listed and have documented quotations and paraphrases as such. The thesis in its current or similar version has not been submitted to an auditing institution before.

15.09.2025

Ort, Datum
(place, date)

Unterschrift
(signature)

Belehrung:
Wer vorsätzlich gegen eine die Täuschung über Prüfungsleistungen betreffende Regelung einer Hochschulprüfungsordnung verstößt, handelt ordnungswidrig. Die Ordnungswidrigkeit kann mit einer Geldbuße von bis zu 50.000,00 € geahndet werden. Zuständige Verwaltungsbehörde für die Verfolgung und Ahndung von Ordnungswidrigkeiten ist der Kanzler/die Kanzlerin der Technischen Universität Dortmund. Im Falle eines mehrfachen oder sonstigen schwerwiegenden Täuschungsversuches kann der Prüfling zudem exmatrikuliert werden. (§ 63 Abs. 5 Hochschulgesetz - HG -).

Die Abgabe einer falschen Versicherung an Eides statt wird mit Freiheitsstrafe bis zu 3 Jahren oder mit Geldstrafe bestraft.

Die Technische Universität Dortmund wird ggf. elektronische Vergleichswerkzeuge (wie z.B. die Software „turnitin") zur Überprüfung von Ordnungswidrigkeiten in Prüfungsverfahren nutzen.

Die oben stehende Belehrung habe ich zur Kenntnis genommen:

Official notification:
Any person who intentionally breaches any regulation of university examination regulations relating to deception in examination performance is acting improperly. This offense can be punished with a fine of up to EUR 50,000.00. The competent administrative authority for the pursuit and prosecution of offenses of this type is the Chancellor of TU Dortmund University. In the case of multiple or other serious attempts at deception, the examinee can also be unenrolled, Section 63 (5) North Rhine-Westphalia Higher Education Act (Hochschulgesetz, HG).

The submission of a false affidavit will be punished with a prison sentence of up to three years or a fine.

As may be necessary, TU Dortmund University will make use of electronic plagiarism-prevention tools (e.g. the "turnitin" service) in order to monitor violations during the examination procedures.

I have taken note of the above official notification:*

15.09.2025

Ort, Datum
(place, date)

Unterschrift
(signature)

*Please be aware that solely the German version of the affidavit ("Eidesstattliche Versicherung")
for the Bachelor's/ Master's thesis is the official and legally binding version.